JGR Oceans

RESEARCH ARTICLE
10.1029/2020JC016112

Quantifying Dynamical Proxy Potential Through Shared Adjustment Physics in the North Atlantic

N. Loose[1,2], P. Heimbach[1,3,4], H. R. Pillar[1], and K. H. Nisancioglu[2,5]

[1]Oden Institute for Computational Engineering and Sciences, The University of Texas at Austin, Austin, TX, USA, [2]Department of Earth Science, University of Bergen, and Bjerknes Centre for Climate Research, Bergen, Norway, [3]Jackson School of Geosciences, The University of Texas at Austin, Austin, TX, USA, [4]Institute for Geophysics, The University of Texas at Austin, Austin, TX, USA, [5]Department of Geosciences, University of Oslo, and Centre for Earth Evolution and Dynamics, Oslo, Norway

Key Points:
- Sensitivities of key metrics, representing observed and desirable quantities in the ocean, are computed using an adjoint model
- Similar sensitivity distributions indicate proxy potential through shared ocean adjustment physics
- In contrast to conventional statistical methods, our quantification of proxy potential is rigorously dynamics-based

Supporting Information:
- Supporting Information S1
- Movie S1
- Movie S2
- Movie S3
- Movie S4
- Movie S5
- Movie S6
- Movie S7
- Movie S8
- Movie S9

Correspondence to:
N. Loose,
nora.loose@utexas.edu

Citation:
Loose, N., Heimbach, P., Pillar, H. R., & Nisancioglu, K. H. (2020). Quantifying dynamical proxy potential through shared adjustment physics in the North Atlantic. *Journal of Geophysical Research: Oceans*, *125*, e2020JC016112. https://doi.org/10.1029/2020JC016112

Received 24 JAN 2020
Accepted 9 AUG 2020
Accepted article online 13 AUG 2020

Abstract Oceanic quantities of interest (QoIs), for example, ocean heat content or transports, are often inaccessible to direct observation, due to the high cost of instrument deployment and logistical challenges. Therefore, oceanographers seek proxies for undersampled or unobserved QoIs. Conventionally, proxy potential is assessed via statistical correlations, which measure covariability without establishing causality. This paper introduces an alternative method: quantifying dynamical proxy potential. Using an adjoint model, this method unambiguously identifies the physical origins of covariability. A North Atlantic case study illustrates our method within the ECCO (Estimating the Circulation and Climate of the Ocean) state estimation framework. We find that wind forcing along the eastern and northern boundaries of the Atlantic drives a basin-wide response in North Atlantic circulation and temperature. Due to these large-scale teleconnections, a single subsurface temperature observation in the Irminger Sea informs heat transport across the remote Iceland-Scotland ridge (ISR), with a dynamical proxy potential of 19%. Dynamical proxy potential allows two equivalent interpretations: Irminger Sea subsurface temperature (i) shares 19% of its adjustment physics with ISR heat transport and (ii) reduces the uncertainty in ISR heat transport by 19% (independent of the measured temperature value), if the Irminger Sea observation is added without noise to the ECCO state estimate. With its two interpretations, dynamical proxy potential is simultaneously rooted in (i) ocean dynamics and (ii) uncertainty quantification and optimal observing system design, the latter being an emerging branch in computational science. The new method may therefore foster dynamics-based, quantitative ocean observing system design in the coming years.

Plain Language Summary To understand the Earth's changing climate, it is important to estimate how much heat the ocean takes up from the atmosphere and how the ocean recirculates the heat around the globe. Directly obtaining these estimates from measurements is complicated because oceanographers cannot measure the ocean everywhere. Ocean measurements taken from ships or freely drifting instruments are expensive and difficult to obtain, especially in regions with ice cover or rough weather conditions. To analyze how existing measurements can be used to estimate unmeasured aspects of the ocean, past studies have used statistical correlations, although it is usually unclear whether correlations have a real, physical origin. This paper introduces a new method: We replace statistical correlations by correlations that have an underlying physical mechanism. As an example, the paper reveals that (A) a subsurface ocean temperature measurement in the Irminger Sea helps to better estimate (B) poleward ocean heat transport across the Iceland-Scotland ridge, hundreds of kilometers away. (A) and (B) are related by physics-based correlation, which is created by a similar dynamical response of (A) and (B) to changes in the near- and far-field wind. The new method can be used to plan effective instrument placements in the future.

1. Introduction

Satellite altimetry and the global array of Argo floats have vastly increased the observational coverage of the world's oceans since the early 1990s (Fu et al., 2018; Riser et al., 2016). Nevertheless, large parts of the ocean remain undersampled in space and time, due to the high cost of instrument deployment, ongoing technical and logistical challenges, and the fact that critically relevant processes occur on a wide range of spatial and temporal scales (e.g., Weller et al., 2019). Therefore, many oceanographic quantities of interest (QoIs) are not directly or continuously measured. Examples are volume, heat, and freshwater transports across many

oceanographic passages, straits, and latitude bands, in particular, the Atlantic meridional overturning circulation (AMOC). Additional QoIs may be ocean heat and freshwater content in regions not well sampled by Argo floats, for example, near the margins or the polar ice sheets. Other examples are strongly related to future societal concerns and key targets for climate predictions. These include future Arctic sea ice cover or regional sea level anomalies. In oceanography, we are therefore on the quest for proxies. That is, it is desirable—and an active part of climate research—to employ observed quantities as proxies for QoIs that are undersampled or unobserved.

Examples of past efforts in this direction include studies which found that anomalies in sea level (available from altimetry) or ocean bottom pressure (available from gravimetry) can serve as a skillful proxy for AMOC variability on interannual time scales (e.g., Bingham & Hughes, 2009; Ezer, 2015; Frajka-Williams, 2015; Landerer et al., 2015; McCarthy et al., 2015). Other studies suggested that, on decadal and longer time scales, North Atlantic surface or subsurface temperature have a characteristic "fingerprint" associated with changes in AMOC and that the (better observed) temperature fingerprint can be used as a proxy for (unobserved) AMOC (e.g., Baehr et al., 2007; Caesar et al., 2018; Knight et al., 2005; Latif et al., 2004; Vellinga & Wood, 2004; Zhang, 2007, 2008). Consequently, available sea level and (sub)surface temperature records have been used to reconstruct AMOC changes back in time (Ezer, 2015; Frajka-Williams, 2015; Lopez et al., 2017; Ritz et al., 2013; Thornalley et al., 2018; Zhang et al., 2015). Moreover, sea surface height, ocean bottom pressure, and hydrographic observations at selected locations have been proposed as a useful observing system to detect AMOC changes in the present ocean and under future climate change scenarios, complementing or substituting current direct North Atlantic transbasin transport measurements, which are limited in space and time (see Frajka-Williams et al., 2019 for a review).

Proxy potential is typically assessed by means of statistical regression or correlation (e.g., see all AMOC proxy studies referenced in the previous paragraph), including regression using statistical modes of variability obtained, for example, via principal component analysis (von Storch & Zwiers, 1999). Figure 1a sketches the concept of evaluating statistical proxy potential: One assesses covariability between an observable quantity (pink time series) and an unobserved QoI (purple time series), often in model output. This method provides an empirical measure for proxy potential but does not identify causal relations. Without dynamical underpinnings, reported dependency on model choice, forcing scenario and time period considered (Alexander-Turner et al., 2018; Little et al., 2019; Roberts & Palmer, 2012) complicates robust identification of proxy potential. The goal of this work is to overcome the limitations of statistical proxy potential. Here, we establish a new methodology that quantifies *dynamical*, rather than statistical, *proxy potential*.

Our goal is to unambiguously identify shared dynamical processes and pathways that provide a mechanistic underpinning for what we will refer to as dynamical proxy potential (DPP). To do so, we take advantage of the adjoint of an ocean general circulation model (GCM). The adjoint can efficiently uncover the dynamical cause of variations in observed and unobserved ocean quantities, extracted from the equations of motion and conservation laws governing the underlying GCM (Marotzke et al., 1999). For instance, adjoint-derived sensitivities have been used to study the dynamical cause of changes in the following QoIs: Atlantic meridional heat transport (Heimbach et al., 2011; Köhl, 2005; Marotzke et al., 1999), AMOC (Czeschel et al., 2010; Heimbach et al., 2011; Pillar et al., 2016; Smith & Heimbach, 2019), Labrador Sea heat content (Jones et al., 2018), temperature in the east equatorial Pacific (Galanti & Tziperman, 2003; Galanti et al., 2002), sea level on the Californian coast and in the Mediterranean Sea (Fukumori et al., 2007; Verdy et al., 2013), and Arctic ocean bottom pressure (Fukumori et al., 2015). Building on previous studies, we exploit the adjoint in a novel fashion, as sketched in Figure 1b: We identify forcings (green shading) affecting both an observed quantity (e.g., temperature in the pink box) and an unobserved QoI (e.g., heat transport across the purple section). By this approach, we find dynamical causes and controls of covariability between the observed and unobserved quantity.

We illustrate the new concept of DPP for a case study in the North Atlantic, choosing heat transport across the Iceland-Scotland ridge (ISR) as our exemplary QoI. The ISR is the key gateway for poleward heat progression from the North Atlantic toward the Arctic Ocean (Hansen & Østerhus, 2000). Warm Atlantic waters are carried across the ridge by the Norwegian Atlantic Current (NwAC), one of the main branches of the North Atlantic Current (NAC; see Figure 2). While observational estimates for ISR heat transport since the mid-1990s exist (e.g., Berx et al., 2013; Hansen et al., 2015; Østerhus et al., 2005, 2019), cross-ridge

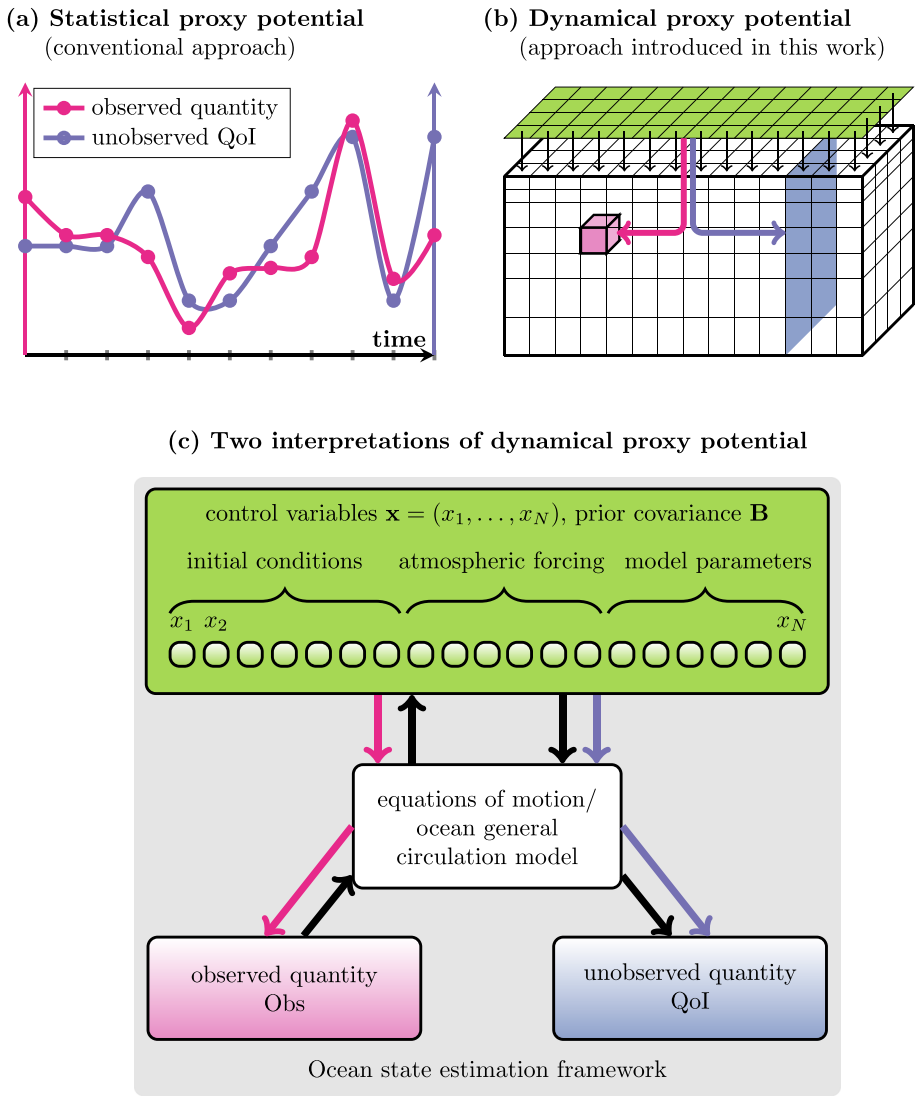

Figure 1. (a and b) Two approaches to assess proxy potential of an observed quantity (pink) for an unobserved quantity of interest (QoI, purple): (a) statistical proxy potential assesses covariability based on empirical evidence; (b) dynamical proxy potential assesses causes (green shading) of covariability based on dynamical laws. (c) Two equivalent interpretations of dynamical proxy potential (see section 2): via (i) shared ocean adjustment physics (pink & purple arrows) and (ii) uncertainty quantification in ocean state estimation (black arrows).

heat transport estimates remain uncertain, due to a sparse array of current meter moorings and the sensitivity to the choice of calculation method (Berx et al., 2013; McCarthy et al., 2019). In contrast, upper ocean temperatures are well constrained throughout the larger part of the North Atlantic basin via remote sensing and in situ platforms. For this reason, we select our representative observed quantities as temperature at the sea surface and at 300 m depth, at two locations in the North Atlantic: in the Irminger Current (IC) and off the Portuguese coast (Figure 2), monitored by the OSNAP (Lozier et al., 2017, 2019) and OVIDE (Lherminier et al., 2007; Mercier et al., 2015) sections, respectively. These locations are intentionally chosen in two branches of the NAC that are distinct from the branch crossing the ISR (Figure 2) and are therefore not expected to be ideal placements for monitoring ISR heat transport. We will show that these observations nevertheless provide partial constraints on the QoI through shared adjustment physics, which are uncovered and quantified by DPP.

Here, we work within the global ECCO (Estimating the Circulation and Climate of the Ocean) Version 4 state estimation framework (Forget et al., 2015) and focus on monthly to multiannual time scales up to 5 years, since now approximately 5 years of continuous OSNAP measurements are available. We note that

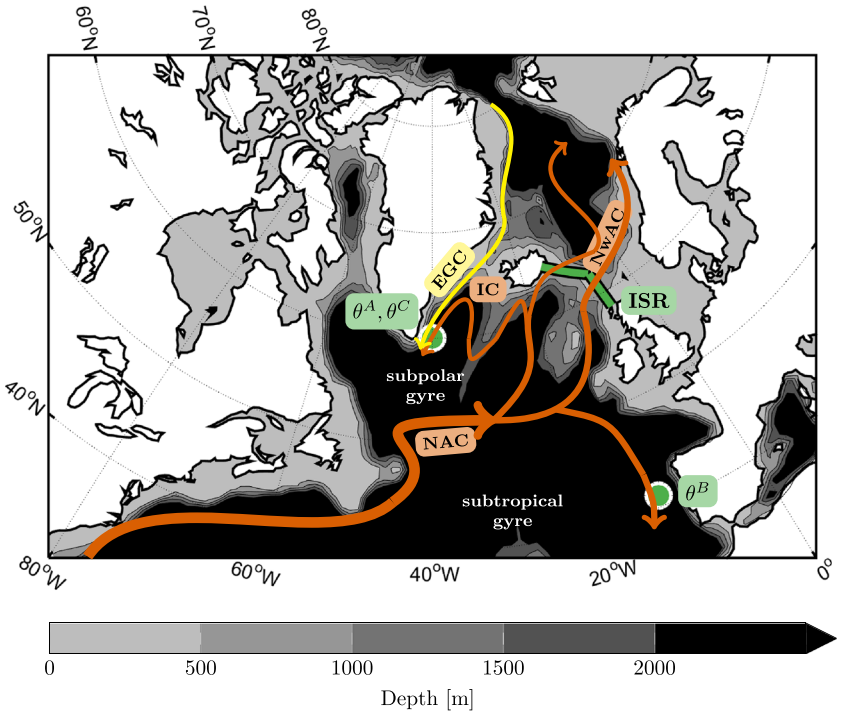

Figure 2. Schematic of the North Atlantic quantities examined in our case study. The quantity of interest (QoI) is heat transport across the Iceland-Scotland ridge (ISR, green line). The temperature observations θ^A, θ^B, and θ^C are located inside the green dots. θ^A and θ^B are subsurface (at 300 m depth), θ^C at the sea surface. The arrows represent approximate pathways of major near-surface currents carrying warm, saline Atlantic waters (orange) and cold, fresh Arctic waters (yellow): NAC = North Atlantic Current; NwAC = Norwegian Atlantic Current; IC = Irminger Current; EGC = East Greenland Current.

assessment of DPP does not require actual (here: OSNAP and OVIDE) observational data, since it investigates dynamical relationships in the model equations, rather than observed covariability. This paper is structured as follows. Section 2 introduces our new method that quantifies DPP. Section 3 applies the methodology to our North Atlantic case study. In section 4, we discuss our results as well as limitations and future directions. Section 5 presents the main conclusions.

2. Quantifying DPP

We define proxy potential of an observed quantity, Obs, for a quantity of interest, QoI, as

$$\mathrm{PP}(\mathrm{Obs};\,\mathrm{QoI}) = \left(\frac{\mathrm{Cov}(\mathrm{Obs},\,\mathrm{QoI})}{\sigma_{\mathrm{Obs}}\cdot\sigma_{\mathrm{QoI}}}\right)^2 \in [0,\,1]. \tag{1}$$

Here, the operators $\mathrm{Cov}(\clubsuit,\spadesuit)$ and $\sigma_{\clubsuit}$ denote covariance and standard deviation, respectively. Conventionally, these operators are evaluated statistically, in which case we refer to Equation 1 loosely as "statistical proxy potential". A statistical evaluation can be performed, for instance, if time series (e.g., from model output) are available, as sketched in Figure 1a; the right-hand side of Equation 1 is then equal to the squared Pearson correlation coefficient, often referred to as r^2. To define and assess DPP, we require a dynamics-based evaluation of the operators in Equation 1. For this, we leverage the framework of ocean state estimation and inbuilt adjoint capability, as described in the following.

Ocean state estimation seeks to infer a best estimate from uncertain (and often sparse) ocean observations and an ocean model with uncertain inputs. The uncertain inputs are also referred to as the control variables, collected in the vector $\mathbf{x} = (x_1, \ldots, x_N)$, and typically consist of spatiotemporal varying atmospheric forcing, initial conditions, and certain model parameters (green box in Figure 1c or Forget et al., 2015). An assigned $N \times N$ covariance matrix $\mathbf{B}$ spells out assumptions on the prior uncertainty in the control variables (Tarantola, 2005; Wunsch, 1996). Ocean state estimation then fits the model to the available observations,

by adjusting (or "inverting" for) the control variables within their prescribed uncertainty. In contrast, the model state variables (within the white centered box, Figure 1c), for example, temperature and velocity, adjust freely in response to the adjusted control variables, following the model dynamics to ensure dynamical and kinematic consistency. An implicit assumption in ocean state estimation is that the control variables comprise all possible sources of changes in the ocean state and circulation.

Ocean state estimation offers a comprehensive framework to quantify proxy potential (Equation 1) and its dynamical origins, where the candidates for proxy origin are formally provided by the control variables. Within this framework, the covariance between Obs and QoI is the scalar

$$\mathrm{Cov}(\mathrm{Obs},\ \mathrm{QoI}) = [\nabla_{\mathbf{x}}\mathrm{QoI}]^T\ \mathbf{B}\ \nabla_{\mathbf{x}}\mathrm{Obs}. \tag{2}$$

Here, the gradient $\nabla_{\mathbf{x}}(\clubsuit) = [\partial(\clubsuit)/\partial x_1, \dots, \partial(\clubsuit)/\partial x_N]^T$ is the vector whose ith component is the linearized sensitivity of the scalar $\clubsuit \in \{\mathrm{QoI}, \mathrm{Obs}\}$ to the control variable x_i, and $[\nabla_{\mathbf{x}}(\clubsuit)]^T$ is its transpose, that is, the associated row vector. The covariance in Equation 2 can be thought of as being computed from right to left–from the observed quantity via the controls to the QoI–, following the black arrows in Figure 1c, by means of the adjoint and tangent linear models (Errico, 1997). Importantly, the resulting covariance is consistent with ocean dynamical laws. These dynamical laws are baked into the gradients in Equation 2 via the chain rule, which passes through the equations of motion that are encoded in the underlying ocean GCM (white centered box, Figure 1c). Similarly to Equation 2, the standard deviation of the quantity $\clubsuit \in \{\mathrm{Obs}, \mathrm{QoI}\}$ is

$$\sigma_{\clubsuit} = \sqrt{[\nabla_{\mathbf{x}}(\clubsuit)]^T\ \mathbf{B}\ \nabla_{\mathbf{x}}(\clubsuit)}. \tag{3}$$

The fact that the expressions in Equations 2 and 3 are the dynamics-based analogue of purely statistically derived covariance and standard deviations was established by Bennett (1985, 1990). The values computed in Equations 2 and 3 would be entries in the so-called representer matrix (Bennett, 2002), if both quantities, Obs and QoI, were part of the model state variables.

Inserting Equations 2 and 3 into Equation 1, and rearranging terms, leads to the notion of DPP, defined as

$$\mathrm{DPP}(\mathrm{Obs};\ \mathrm{QoI}) = \left(\underbrace{\left[\sigma_{\mathrm{QoI}}^{-1} \cdot \mathbf{B}^{1/2}\ \nabla_{\mathbf{x}}\mathrm{QoI}\right]}_{=\ \mathbf{q}} \bullet \underbrace{\left[\sigma_{\mathrm{Obs}}^{-1} \cdot \mathbf{B}^{1/2}\ \nabla_{\mathbf{x}}\mathrm{Obs}\right]}_{=\ \mathbf{v}} \right)^2 \in [0,\ 1], \tag{4}$$

where $\mathbf{B}^{1/2}$ is the $N \times N$ matrix, which satisfies $\mathbf{B}^{1/2}\mathbf{B}^{1/2} = \mathbf{B}$, and $\bullet$ denotes the dot product in $\mathbb{R}^N$. The bounds in Equation 4 correspond to the cases for which Obs provides *no* information (DPP = 0) and serves as a *perfect* proxy (DPP = 1) for the QoI, similar to the statistics-derived r^2. The vectors $\mathbf{q}$ and $\mathbf{v}$ (defined in Equation 4) contain the sensitivities of QoI and Obs to all controls, allowing for two equivalent interpretations: (i) $\mathbf{q}$ and $\mathbf{v}$ reveal the dynamical adjustment mechanisms of QoI and Obs, respectively (sections 3.2 and 3.3); (ii) $\mathbf{q}$ specifies the *information required* to recover the QoI, while $\mathbf{v}$ is the *information captured* by the observed quantity. Interpretation (ii) is rooted in Hessian uncertainty quantification (UQ) and optimal observing system design within ocean state estimation. This link to UQ is derived in the supporting information (Text S1) and further explored in a forthcoming paper. In the definition of $\mathbf{q}$, $\mathbf{v}$ (Equation 4), multiplication with the matrix $\mathbf{B}^{1/2}$ (prior-)weights the sensitivity vectors $\nabla_{\mathbf{x}}(\clubsuit)$, and division by the scalar $\sigma_{\clubsuit}$ acts as normalization. Indeed, Equation 3 can be rewritten as the l^2-norm of the weighted sensitivity vector:

$$\sigma_{\clubsuit} = \mathbf{B}^{1/2}\ \nabla_{\mathbf{x}}(\clubsuit) \tag{5}$$

Figure 1c offers a schematic summary of understanding DPP(Obs;QoI) in line with our two equivalent interpretations. DPP of an observed quantity, Obs (pink box), for an unobserved QoI (purple box), measures the following:

(i) the similarity between the ocean adjustment physics for the observed versus unobserved quantity (pink vs. purple arrows) in response to changes in forcing (green box), on a scale from 0% (*no similarity*) to 100% (*identical*);

(ii) the relative uncertainty reduction in the QoI that would be achieved if the observation were to be added without noise to the state estimation framework in Figure 1c (see Text S1). The flow of information and uncertainty reduction within the state estimation framework—from the observation via the controls to the QoI—is delineated by the black arrows.

3. Application to the North Atlantic

This section illustrates our method for a case study in the North Atlantic. Section 3.1 describes the experimental setup, including our choice of QoI and observations. Sections 3.2 and 3.3 present the adjustment mechanisms of the QoI and observations. Section 3.4 assesses the degree to which these adjustments are shared and quantifies the DPP of the observations for the QoI.

3.1. Experimental Setup

We perform our experiments using the ECCO Version 4 Release 2 (ECCOv4r2; Forget et al., 2015) solution. The Massachusetts Institute of Technology GCM (MITgcm, Marshall, Adcroft, et al., 1997; Marshall, Hill, et al., 1997) serves as the dynamical core in ECCO and is configured at a nominal horizontal resolution of 1° with 50 vertical levels. The optimized state provides an acceptable fit to most available oceanographic data and has been used extensively for mechanistic investigations of ocean variability, including in the North Atlantic (e.g., Buckley et al., 2014; Jones et al., 2018). We refer the reader to Forget et al. (2015) for details on the model configuration and estimated ocean state.

To quantify DPP and its origins, one requires the linear sensitivities of the QoI and observed quantities to all control variables ($\nabla_{\mathbf{x}}$QoI and $\nabla_{\mathbf{x}}$Obs; Equation 4). To perform these sensitivity calculations, we take advantage of the flexible ECCOv4 adjoint modeling framework (Forget et al., 2015). Algorithmic differentiation, through source-to-source code transformation with the commercial tool Transformation of Algorithms in Fortran (TAF; Giering & Kaminski, 1998), produces the code for our adjoint models. Ice-covered regions are masked in the sensitivity calculation.

3.1.1. QoI and Observations

The QoI in our case study is heat transport across the ISR, denoted by $\mathrm{HT_{ISR}}$. We investigate three different temperature observations in the North Atlantic, located inside the green dots in Figure 2 and labeled by θ^A, θ^B, and θ^C. Observations θ^A and θ^C are located in the Irminger Sea at (40°W, 60°N), while observation θ^B is situated in the eastern North Atlantic off the Portuguese coast at (12°W, 41°N). θ^A and θ^B are subsurface observations, situated at 300 m depth, and θ^C is a surface observation.

We quantify the DPP of the 5 year mean of the observations for the 5 year mean of our QoI, for zero lag. Sensitivities of the QoI and observations (Equation 4) are computed from the final 5 years (2007–2011) of the ECCOv4r2 state estimate. Dependence on the specific evaluation period and background state is weak, given that $\mathrm{HT_{ISR}}$, θ^A, θ^B, and θ^C depend approximately linearly on the control variables (Appendix A).

The QoI, as simulated by the model, is diagnosed as follows:

$$\mathrm{HT_{ISR}} = \frac{\rho_0\, c_p}{\Delta t} \int_{2007}^{2011} \int_{\mathrm{bottom}}^{\mathrm{top}} \int_L (\theta - \theta_{\mathrm{ref}})\, v^{\perp}\, dL\, dz\, dt \quad (W). \tag{6}$$

L denotes the Iceland-Faroe-Scotland line segment, $\Delta t = \int_{2007}^{2011} dt$ the length of the integration period, $\rho_0 = 1{,}029\ \mathrm{kg/m^3}$ the reference density, and $c_p = 3994\ \mathrm{J/(kg{\cdot}K)}$ the specific heat capacity of water. θ denotes potential temperature, and $v^{\perp}$ the velocity perpendicular to the line segment L; sign convention is such that positive $v^{\perp}$ corresponds to positive northward and eastward velocity. Note that since L is only a partial line segment, rather than a closed boundary, heat transport in Equation 6 has to be defined relative to a reference temperature θ_{ref} (Schauer & Beszczynska-Möller, 2009). Consistent with many observational studies (e.g., Berx et al., 2013; Hansen et al., 2015; Østerhus et al., 2005), we choose $\theta_{\mathrm{ref}} = 0°C$, motivated by the observation that southward flow across the ISR is close to this temperature (Hansen et al., 2003).

For $\star \in \{A, B, C\}$, the observation $\theta^\star$ is diagnosed as the mean potential temperature

$$\theta^\star = \frac{1}{\Delta t \cdot \mathscr{V}^\star} \int_{2007}^{2011} \int_{h_0^\star}^{h_1^\star} \int_{\mathscr{A}^\star} \theta\, dx\, dy\, dz\, dt \quad (°\mathrm{C}). \tag{7}$$

$(h_0)^\star$, $(h_1)^\star$, and $\mathscr{A}^\star$ denote the lower and upper boundaries, and the horizontal area, of the model grid cell in which the respective observation $\theta^\star$ is located. For the subsurface observations ($\star = A, B$), we

Table 1
Control Variables and Weights in our Case Study.

m	Forcing $F_m(i,j)$	Symbol	Time average	ΔF_m
1	Net upward surface heat flux	$Q_{\text{net},\uparrow}$	5 years	$50\,\text{W/m}^2$
2	Net surface freshwater flux	EPR	5 years	$5\cdot10^{-8}$ m/s
3	Zonal wind stress	τ_x	5 years	$0.05\,\text{N/m}^2$
4	Meridional wind stress	τ_y	5 years	$0.05\,\text{N/m}^2$

have $(h_0)^\star = -325$ m and $(h_1)^\star = -275$ m. For the surface observation, we choose the uppermost two model grid cells as a representative depth range, corresponding to $(h_0)^C = -20$ m and $(h_1)^C = 0$ m. The area of $\mathscr{A}^A = \mathscr{A}^C$ is approximately $(52\,\text{km})^2$ and the area of $\mathscr{A}^B$ is approximately $(84\,\text{km})^2$. In Equation 7, $\theta(x,y,z,t)$ denotes potential temperature, $\Delta t = \int_{2007}^{2011} dt$ the length of the integration period, and $\mathscr{V}^\star = \int_{h_0^\star}^{h_1^\star}\int_{\mathscr{A}^\star} dx\,dy\,dz$ the volume of interest.

3.1.2. Control Variables and Weights

Table 1 lists the set of control variables that is chosen in this work: the spatially varying forcing fields $F_m(i,j)$ of net upward surface heat flux, $Q_{\text{net},\uparrow}$, net surface freshwater flux, EPR, and zonal and meridional wind stress, τ_x and τ_y, respectively. Consistent with assessing DPP of the 5 year mean of the observations for the 5 year mean of the QoI, only adjustments to changes in the 5 year mean of the forcing fields are considered (fourth column, Table 1). For the sake of a simpler presentation, initial conditions and model parameter fields are omitted, even though they are part of the uncertain inputs in a full ocean state estimation framework (green box, Figure 1c). The four two-dimensional forcing fields are flattened and concatenated into a long vector, $\mathbf{x} = (x_1, \dots, x_N)$. The length of the vector, N, is $O(10^6)$, equal to 4 times the number of model surface grid cells covering the global ocean.

For each of the four forcing fields, F_m, we set a spatially constant prior standard deviation, ΔF_m (last column, Table 1). Further, we assume the decorrelation length in the surface forcing to be less than the grid scale ($\sim 1°$). Meanwhile, ECCOv4r2 uses spatially varying prior standard deviations, estimated based on the spread between different reanalysis products (Chaudhuri et al., 2013) and sets a decorrelation length of 3 times the grid scale within the same forcing field (but no cross correlations between distinct forcing fields, Forget et al., 2015). Our choices correspond to a diagonal prior covariance $\mathbf{B}$, and its square root is the diagonal $N\times N$ matrix

$$\mathbf{B}^{1/2} = \text{diag}\left(\underbrace{\Delta F_1,\ \dots,\ \Delta F_1}_{N/4\ \text{times}}, \underbrace{\Delta F_2,\ \dots,\ \Delta F_2}_{N/4\ \text{times}}, \underbrace{\Delta F_3,\ \dots,\ \Delta F_3}_{N/4\ \text{times}}, \underbrace{\Delta F_4,\ \dots,\ \Delta F_4}_{N/4\ \text{times}}\right). \tag{8}$$

Our assumption of spatially uniform weights ΔF_m and no prior spatial cross correlations implies that the sensitivity projection (Equation 4) for each individual forcing field is fully determined by the adjustment physics, and not by the forcing weights. Our simplified choice of forcing covariance therefore adds clarity to the presentation in this paper, whose primary goal is to explain the new concept of DPP.

3.2. Adjustment Mechanisms of the QoI

Figures 3a–3d show the weighted and normalized sensitivities of the 5 year mean heat transport across the ISR (HT_{ISR}):

$$\mathbf{q}_{|F_m(i,j)} = \sigma_{\text{HT}}^{-1}\frac{\partial(\text{HT}_{\text{ISR}})}{\partial F_m(i,j)}\Delta F_m, \qquad m = 1,\ 2,\ 3,\ 4. \tag{9}$$

Here, $F_m(i,j)$ are the 5 year mean atmospheric forcing fields from Table 1, and ΔF_m their spatially uniform weights. The normalization factor, $\sigma_{\text{HT}} = 6TW$, is computed according to Equations 5 and 8, with $\clubsuit = \text{HT}_{\text{ISR}}$. The weighted and normalized sensitivities of HT_{ISR} in Equation 9 (or Figures 3a–3d) assemble the vector $\mathbf{q}$ (cf. Equations 4 and 8), which has two equivalent interpretations (section 2): (i) $\mathbf{q}$ reveals all adjustment mechanisms of HT_{ISR}, as will be discussed in the following paragraphs; (ii) $\mathbf{q}$ is the information required

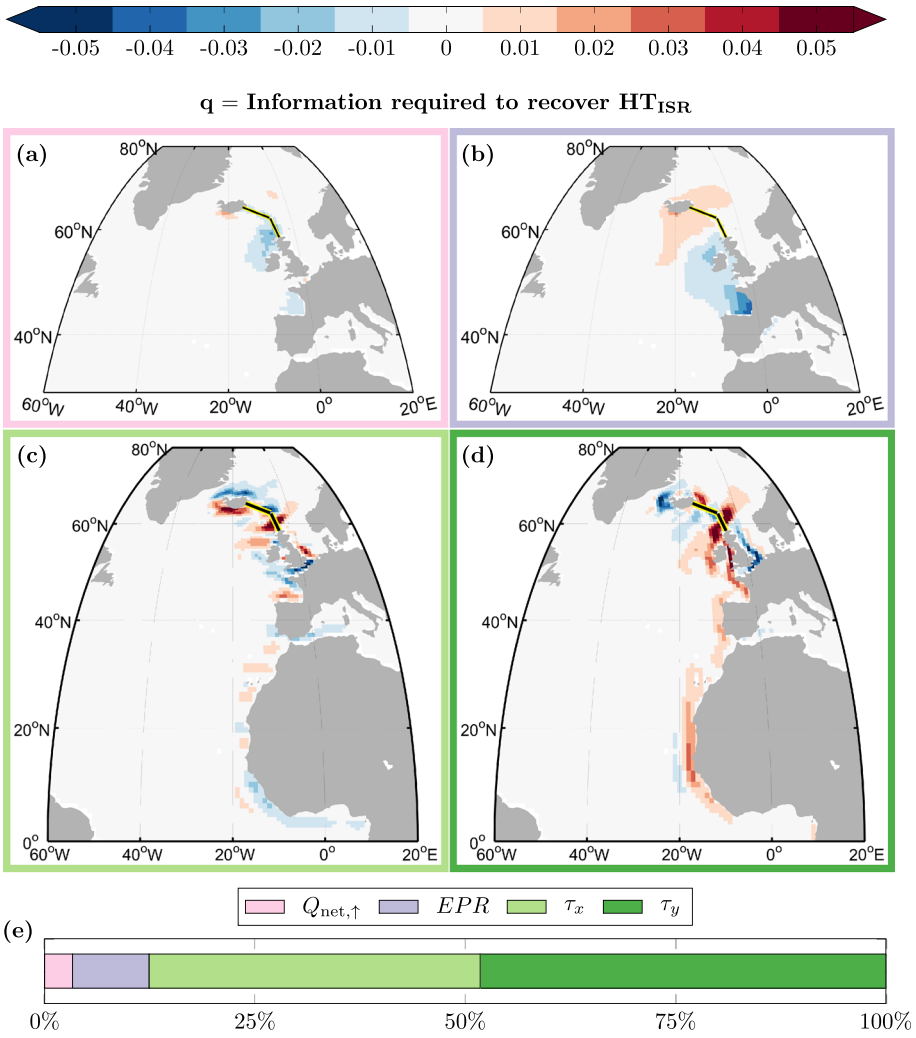

Figure 3. Sensitivities of 5 year mean heat transport across the Iceland-Scotland ridge (HT_{ISR}), to changes in the 5 year mean (a) upward surface heat flux $Q_{net,\uparrow}$, (b) surface freshwater flux *EPR*, (c) zonal wind stress τ_x and (d) meridional wind stress τ_y. The sensitivities are weighted and normalized (thus unitless) and assemble the vector **q** (Equation 9). Red (blue) colors indicate that an increase in (a) heat loss to the atmosphere, (b) surface salinification, (c) eastward wind stress, and (d) northward wind stress would lead to a subsequent increase (decrease) in HT_{ISR} on a 5 year time scale. The solid black-yellow contour in (a)–(d) delineates the ISR. The bar chart in (e) shows the relative contributions of $Q_{net,\uparrow}$, *EPR*, τ_x and τ_y to HT_{ISR} sensitivity, when integrating the sensitivities in (a)–(d) around the globe (Equation 10).

to recover HT_{ISR}, our QoI. The bar chart in Figure 3e shows the relative importance of the four forcings F_m for impacting HT_{ISR}. Relative importance is measured by the ratios

$$\left\|\mathbf{q}_{|F_m}\right\|^2 = \sigma_{HT}^{-2} \sum_{i,j} \left(\frac{\partial(HT_{ISR})}{\partial F_m(i,j)} \Delta F_m\right)^2, \qquad m = 1, 2, 3, 4, \tag{10}$$

equivalent to integrating the sensitivities in Figures 3a–3d around the globe (in the l^2-norm). Figure 3e demonstrates that the influence of wind stress, τ_x and τ_y, prevails over the influence of buoyancy forcing, $Q_{net,\uparrow}$ and *EPR*.

The positive sensitivity of HT_{ISR} to τ_y along the western African and European coast (Figure 3d) is consistent with the following dynamical mechanism. An increase in northward wind stress along the western African and European coast induces Ekman onshore convergence and a positive pressure anomaly along the coast. Boundary waves (e.g., Marshall & Johnson, 2013) propagate the positive pressure anomaly cyclonically around the North Atlantic basin (Figure 5a). When the positive pressure anomaly reaches the eastern end

of the ISR (within a month, see Movie S1), it leads to an increased along-ridge pressure gradient and, by geostrophic balance, a strengthened HT_{ISR}. While the HT_{ISR} anomaly develops rapidly (after a few months, Figure A1b), it persists for as long as the wind stress perturbation is maintained (here: for 5 years). The sensitivity to zonal wind stress along the western African and European coastline (Figure 3c) is due to the same mechanism. Here, the sensitivity sign alternates because it is determined by the orientation of the coastline.

The wind stress sensitivities of HT_{ISR} around Iceland and the United Kingdom (U.K.) that emerge in Figures 3c and 3d can be explained similarly. By way of illustration, *negative* sensitivity of HT_{ISR} to τ_y along the western coast of Iceland (Figure 3d) is consistent with the following mechanism. An increase in northward wind stress along the western Icelandic coast drives Ekman onshore convergence, resulting in a positive pressure anomaly at the Icelandic coast. Through clockwise wave propagation around the Icelandic coastline, the positive pressure anomaly is rapidly communicated to the western end of the ISR (Figure 5b and Movie S7). The resulting negative anomaly in the along-ridge pressure gradient leads to a *weakening* of HT_{ISR} and, consequently, colder temperatures in the Norwegian Sea (Figure 5d). As before, the HT_{ISR} anomaly develops rapidly but persists for 5 years (Figure A1d). This mechanism also explains the sign of the τ_x sensitivities around Iceland: increased eastward (westward) wind stress along the southern (northern) coast of Iceland (Figure 3c) drives Ekman offshore divergence, resulting in a negative pressure anomaly at the Icelandic coast and a subsequent increase in HT_{ISR}. Since the U.K. coastline delivers pressure signals to the eastern (rather than the western) end of the ISR, U.K.-originated pressure anomalies increase HT_{ISR} if they are positive (rather than negative). This explains the fact that the sensitivity dipoles around Iceland and the U.K. are of opposite sign (Figures 3c and 3d).

HT_{ISR} shows positive sensitivity to $Q_{net,\uparrow}$ and *EPR* to the west of the ISR, around Iceland, and negative sensitivity to the east of the ISR, along the western European coast (Figures 3a and 3b). This sensitivity dipole across the core of the NAC is consistent with a strengthening of the cross-ridge geostrophic transport in response to a negative perturbation of the density gradient along the section. The sensitivity of HT_{ISR} to $Q_{net,\uparrow}$, relative to the remaining forcing fields, is surprisingly small: only 3% (Figure 3e). We note that even if we tripled ΔQ_{net} in Table 1, while keeping the weights for the remaining forcings unchanged, HT_{ISR} would still be less sensitive to $Q_{net,\uparrow}$ than to any of the remaining three forcing fields in Figure 3e. This is consistent with previous observation- and model-based studies, which found that on seasonal to multiannual time scales ISR heat transport variability is predominantly driven by velocity fluctuations, rather than temperature fluctuations (Årthun & Eldevik, 2016; Asbjørnsen et al., 2019; Orvik & Skagseth, 2005).

3.3. Adjustment Mechanisms of the Observations

The weighted and normalized sensitivities of the 5 year mean temperature observations $\theta^\star$, $\star = A, B, C$, are given by

$$\mathbf{v}^\star_{[F_m(i,j)} = \sigma_\star^{-1} \frac{\partial \theta^\star}{\partial F_m(i,j)} \Delta F_m, \qquad m = 1, 2, 3, 4, \tag{11}$$

similar to Equation 9. The normalization factors $\sigma_\star$ are computed according to Equations 5 and 8, with $\clubsuit = \theta^\star$, giving $\sigma_A = 0.05°C$, $\sigma_B = 0.06°C$, and $\sigma_C = 0.23°C$. Note that σ_C is much larger than σ_A and σ_B since the surface temperature θ^C is more sensitive to atmospheric forcing than the subsurface temperatures θ^A,θ^B. Figures 4a–4f show the weighted and normalized sensitivities (Equation 11) for two of the four forcings, $F_1 = Q_{net,\uparrow}$ and $F_4 = \tau_y$. The vector $\mathbf{v}^\star$, composed of the weighted and normalized sensitivities in Equation 11, has again two equivalent interpretations: (i) $\mathbf{v}^\star$ reveals the adjustment mechanisms of $\theta^\star$, which will be discussed in the following; (ii) $\mathbf{v}^\star$ is the information captured by the observation $\theta^\star$. The bar charts in Figures 4g–4i show the relative importance of the four forcings F_m for impacting $\theta^\star$, for $\star = A, B, C$. Relative importance is measured as in Figure 3e, by the ratios in Equation 10, where $\mathbf{q}$ is substituted by $\mathbf{v}^\star$.

The relative importance of $Q_{net,\uparrow}$ is high for the surface observation θ^C (Figure 4i), but low for the subsurface observations θ^A and θ^B (Figures 4g and 4h). The high sensitivity of θ^C to $Q_{net,\uparrow}$ is concentrated at the observed site (Figure 4c), due to the strong influence of local air-sea heat fluxes on surface temperature. All temperature observations show weak negative $Q_{net,\uparrow}$ sensitivity upstream of the respective observed sites (Figures 4a–4c), as an increased upward heat flux locally cools surface waters, which are then advected to the observed locations (Figure 2). For all three temperature observations, the relative importance of *EPR* is very small (Figures 4g–4i). Wind stress is important for all three observations (Figures 4g–4i), and the remainder

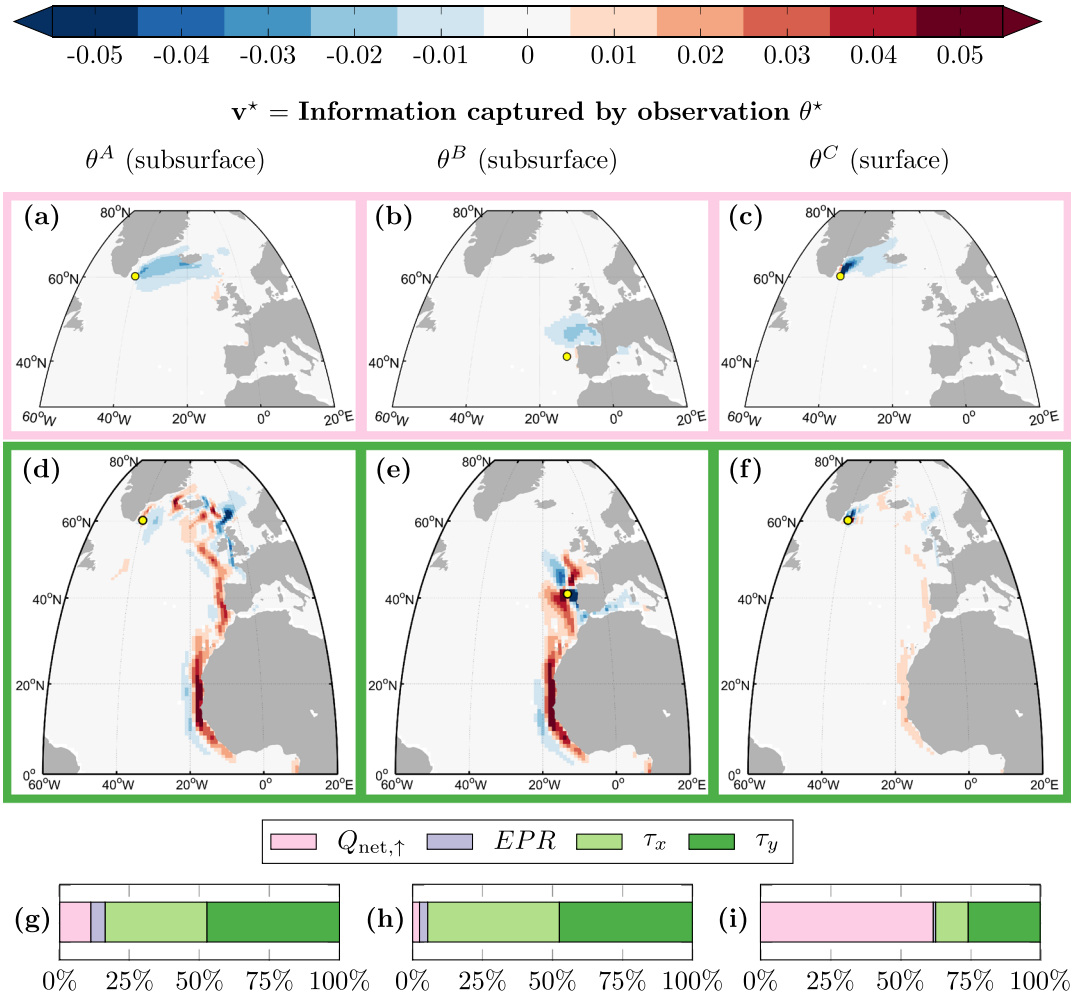

Figure 4. (a–c) Sensitivities of 5 year mean (a) subsurface temperature in the Irminger Sea (θ^A), (b) subsurface temperature off the Portuguese coast (θ^B), and (c) surface temperature in the Irminger Sea (θ^C), to changes in 5 year mean upward surface heat flux $Q_{\text{net},\uparrow}$. (d–f) Same as (a)–(c), but sensitivities to meridional wind stress τ_y. The sensitivities are weighted and normalized (thus unitless) and assemble the vector $\mathbf{v}^\star$ (Equation 11). Red (blue) colors indicate that an increase in (a)–(c) heat loss to the atmosphere and (d)–(f) northward wind stress would lead to a subsequent increase (decrease) in (a and d) θ^A, (b and e) θ^B, and (c and f) θ^C on a 5 year time scale. The yellow dots mark the respective locations of the temperature observation. The bar charts in (g)–(i) show the relative contributions of $Q_{\text{net},\uparrow}$, *EPR*, τ_x, and τ_y to (g) θ^A, (h) θ^B, and (i) θ^C sensitivity, computed as in Figure 3.

of this section is devoted to wind stress sensitivities. For the sake of brevity, we focus on τ_y sensitivities, which can be regarded as representative for τ_x sensitivities, too. Indeed, τ_x and τ_y sensitivities emerge along the same pathways (not shown) due to the same wind-driven adjustment mechanisms.

All observations are characterized by a sensitivity dipole local to the observed site, consistent with Ekman dynamics. For instance, at (12°W, 41°N), right where θ^B is located, a sensitivity dipole is visible, with positive sensitivities to the west and negative sensitivities to the east (Figure 4e), interrupting the otherwise positive sensitivities along the eastern boundary of the North Atlantic. Here, Ekman theory predicts that a wind stress perturbation matching the sensitivity dipole (i.e., increased northward wind stress to the west and increased southward wind stress to the east) causes Ekman downwelling and pumps warm surface waters down to the subsurface observation, which increases θ^B.

The large-scale wind stress sensitivity patterns of θ^C (Figure 4f) are very similar to the ones of θ^A (Figure 4d), except that they are of much weaker amplitude. The similarity of the patterns suggests that the surface observation θ^C is sensitive to similar remote wind-driven adjustment mechanisms as the subsurface observation

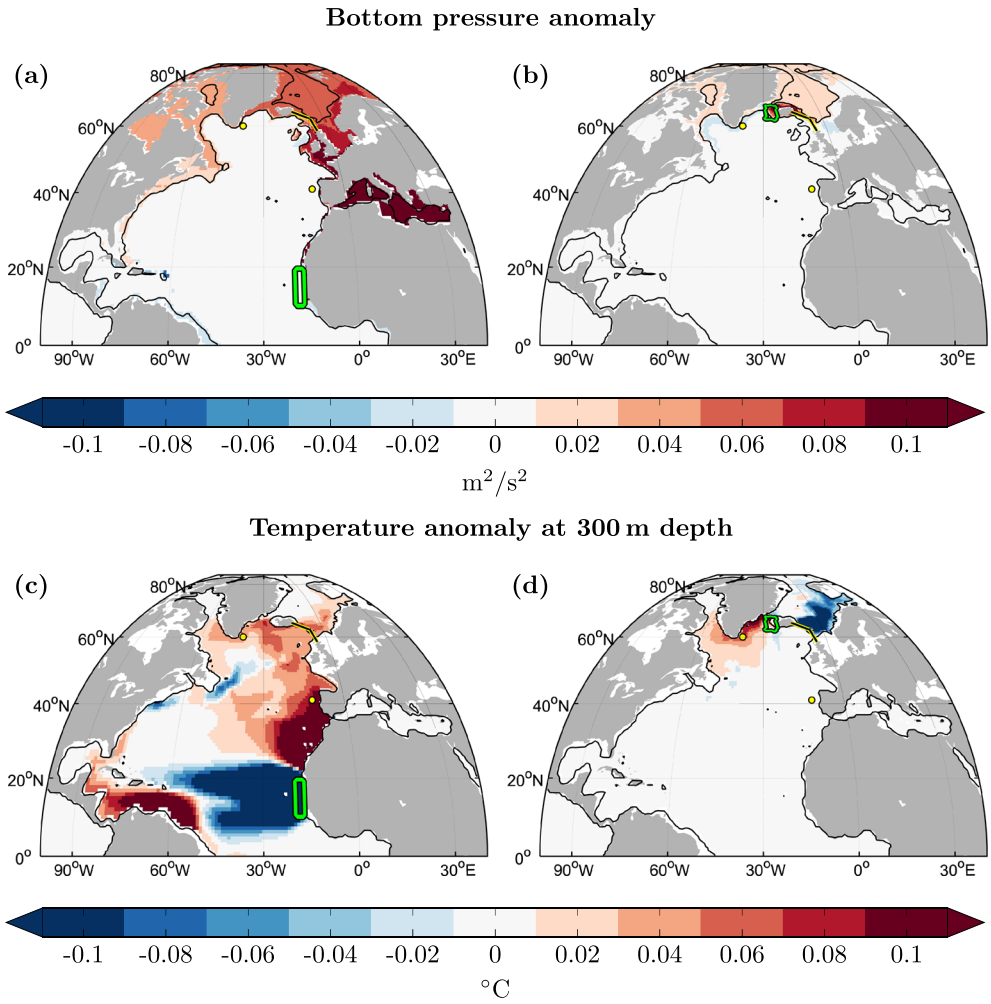

Figure 5. Anomaly in North Atlantic (a and b) bottom pressure (normalized by density, p/ρ) and (c and d) potential temperature at 300 m depth, in response to a positive northward wind stress anomaly of amplitude 0.05 N/m^2 along the (a and c) western African coast and (b and d) western Icelandic coast. The wind stress perturbations are imposed inside the green contour in (a)–(d) and maintained over 5 years. The anomalies shown are time-averaged over the same 5 year time period. The black line marks the (a and b) 1,000 m, (c and d) 300 m depth contour. The yellow dots and black-yellow line show the locations of the temperature observations θ^A, θ^B, and the Iceland-Scotland ridge. Movies of the monthly evolution of these anomalies are shown in the supporting information (Movies S1, S7, S3, and S9).

θ^A. However, local forcing massively dominates the surface temperature response, as indicated by the strong sensitivities concentrated near (40°W, 60°N) in Figures 4c and 4f.

For all three temperature observations, positive sensitivity to northward wind stress emerges along the western African and European coastline (Figures 4d–4f), similar to what was seen for HT_{ISR} in section 3.2. To explain the underlying mechanism, we perform a perturbation experiment, in which the final 5 years of the ECCOv4r2 solution serve as our control simulation. We increase northward wind stress in the region highlighted in Figures 5a and 5c, along the western African coast, by 0.05 N/m^2, and maintain the perturbation over the full 5 year period. Figure 5c shows the response anomalies in subsurface temperature, at a depth of 300 m, time-averaged over the 5 year experiment. We see that, in response to the positive northward wind stress anomaly along the western African coast,the northeast Atlantic (north of 25°N) experiences anomalous high temperatures.

The responsible mechanism operates exactly as demonstrated by Jones et al. (2018), see their Figure 10. The northward wind stress anomaly creates a positive pressure anomaly along the eastern boundary of the North Atlantic, which, after cyclonic propagation around the basin, sets up an anomalous pressure gradient

between the Nordic Seas and the North Atlantic (Figure 5a and Movie S1). The basin-scale pressure gradient along the northern boundary of the North Atlantic spins up the subpolar gyre (Movie S2), leading to a warming of the subpolar North Atlantic after 1–2 years (Figures 5c and A1a and Movie S3). The large-scale warming in the subtropical North Atlantic, north of 25°N (Figure 5c), is the result of baroclinic Rossby waves propagating a warm temperature anomaly from the eastern boundary westward (Movies S3 and S4). The anomalous warming includes the locations of the temperature observations θ^A, θ^B, and θ^C (yellow dots, Figure 5c), explaining the consistently positive sensitivities along the western African coast in Figures 4d–4f. Other accompanying temperature adjustments—most notably, the cooling in the subtropical gyre south of 20°N (Figure 5c and Movies S3 and S6)—do not impact the temperature observations (nor the QoI, HT_{ISR}) on a 5 year time scale but may come into play on longer time scales.

The Irminger Sea observations also show sensitivity to wind stress in the northeastern Atlantic, between 50°N and 70°N (Figures 4d and 4f). In this region, τ_y sensitivities of θ^A, θ^C (Figures 4d and 4f) have a similar pattern as τ_y sensitivities of HT_{ISR} (Figure 3d), except that sensitivities of θ^A, θ^C are of opposite sign to those of HT_{ISR} (see Figures 6c and 6d for a side-by-side comparison). To explain the opposite signs, we perform a second perturbation experiment similar to the one presented in Figures 5a and 5c. In the second experiment, we increase northward wind stress along the western Icelandic coast, in the region highlighted in Figures 5b and 5d, where θ^A and θ^C show positive sensitivity (Figures 4d and 4f) and HT_{ISR} shows negative sensitivity (Figure 3d). Figure 5d shows the response anomaly in subsurface temperature, at a depth of 300 m. The Irminger and Labrador Seas experience a warming, while the Norwegian Sea cools.

The underlying mechanism is the following: the northward wind stress anomaly along the western Icelandic coast drives Ekman onshore convergence and a positive pressure anomaly, as discussed in section 3.2. The positive pressure anomaly is rapidly communicated along the entire Icelandic coastline, resulting in an across-bathymetry pressure gradient (Figure 5b and Movie S7), which drives an anomalous clockwise barotropic circulation around Iceland (Movie S8). The anomalous clockwise circulation around Iceland weakens the northward transport across the ISR by the NwAC as well as the southward transport through Denmark Strait by the EGC, while strengthening the IC (cf. Figure 2). The weakened northward transport of warm Atlantic waters across the ISR leads to the anomalous cold temperatures that are seen in the Norwegian Sea in Figure 5d (and Movie S9) and is consistent with a reduced HT_{ISR}, as predicted by the *negative* sensitivities in Figure 3d. The weakened southward transport of cold Arctic waters through Denmark Strait, together with the strengthened IC, results in the anomalous warming that is seen in the Irminger and Labrador Seas in Figure 5d (see also Figure A1c and Movie S9). The increased temperature in the Irminger Sea is consistent with the *positive* sensitivities along the western Icelandic coast in Figures 4d and 4f.

The perturbation experiment presented in Figures 5b and 5d explains the opposite sign in the sensitivities along the western Icelandic coast in Figure 3d versus Figure 4d. The fact that in Figure 3d versus Figure 4d, sensitivities are *consistently* of opposite sign in the northeast Atlantic between 50°N and 70°N can be understood similarly. The sensitivity patterns in this region are characterized by topographically steered bands, which connect to Iceland or the ISR (Figures 3d and 4d). The sensitivity patterns have opposite sign in Figure 3d versus Figure 4d because wind stress in this region creates pressure anomalies that are transported to the Icelandic coastline. Once there, the pressure anomalies drive a simultaneous strengthening (or weakening) of the NwAC and EGC, as described before, which results in opposite temperature responses in the Irminger versus Norwegian Sea, similarly as in Figure 5d.

3.4. Assessing Shared Adjustment Mechanisms

This section quantifies the DPP of each of the three temperature observations, θ^A, θ^B, and θ^C, for our QoI, heat transport across the ISR (HT_{ISR}). Quantification is via the pointwise projection of sensitivities:

$$\mathbf{q} \cdot \mathbf{v}^{\star} = \sum_{m=1}^{4} \sum_{i,j} \left(\sigma_{\mathrm{HT}}^{-1} \frac{\partial(\mathrm{HT_{ISR}})}{\partial F_m(i,j)} \Delta F_m \right) \cdot \left(\sigma_{\star}^{-1} \frac{\partial \theta^{\star}}{\partial F_m(i,j)} \Delta F_m \right), \tag{12}$$

for $\star = A, B, C$, see Equations 4, 9, and 11. Shared adjustment physics result in strong projections, elucidating the dynamical origins of proxy potential.

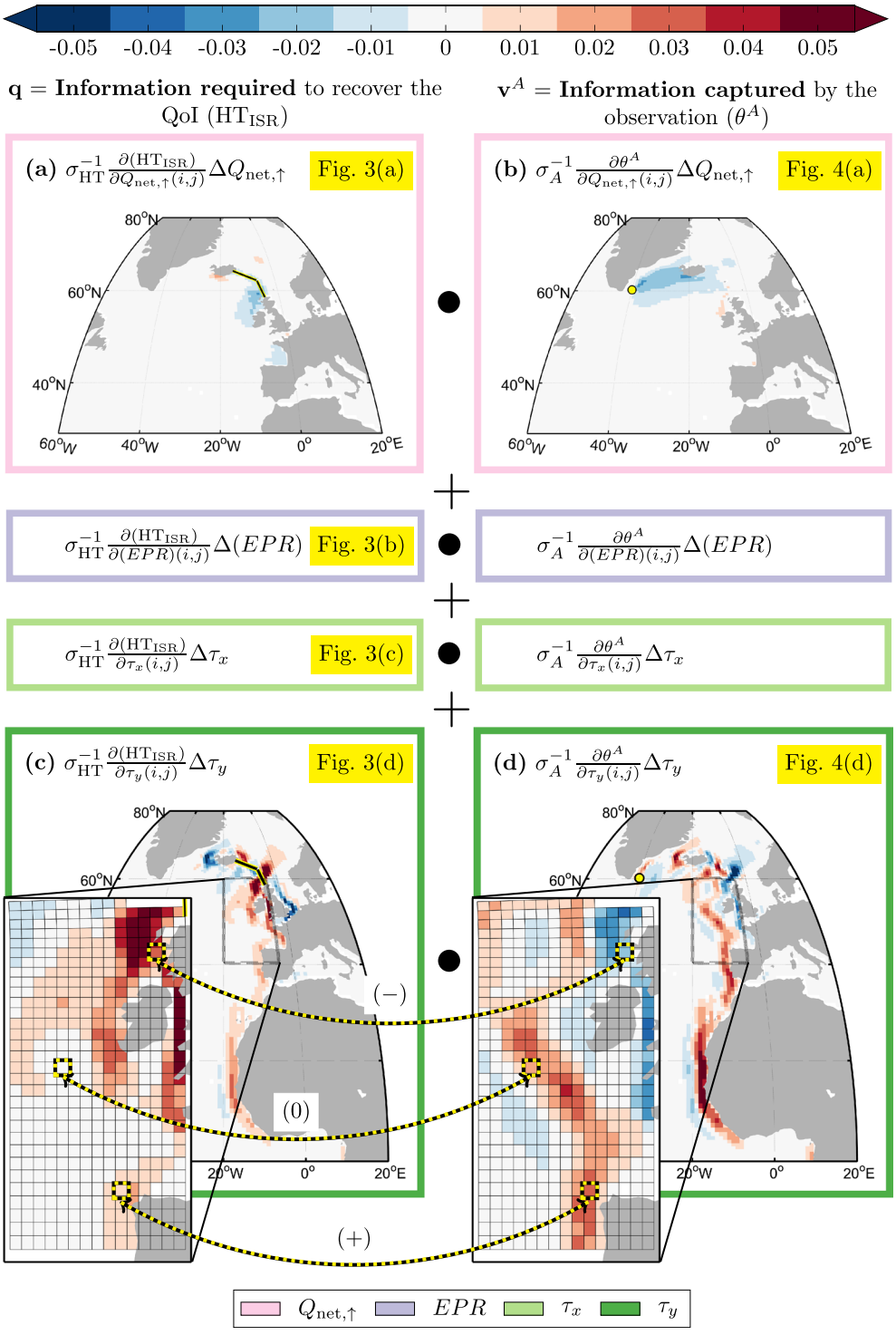

Figure 6. Projection (•) of weighted and normalized sensitivities (Equation 12) of the QoI, $\mathrm{HT}_{\mathrm{ISR}}$ (**q**, left column), and the observed quantity, θ^A ($\mathbf{v}^A$, right column). All shown sensitivity maps are replots of subpanels in Figures 3 and 4, as indicated by the yellow labels, and are composed of patterns that are established by the dynamical adjustment mechanisms of $\mathrm{HT}_{\mathrm{ISR}}$ and θ^A, respectively. Shared adjustment physics result in a strong projection (or "pattern correlation"), elucidating the dynamical origins of proxy potential. The color shading in each of the shown model grid cells (inlets in (c) and (d)) corresponds to an entry in either of the two sensitivity vectors, **q** and $\mathbf{v}^A$, associated with the forcing variable τ_y. The three cases (+), (−), and (0), resulting from the elementwise projection, are discussed in the text.

Figure 6 shows the projection in Equation 12 for the case $\star = A$. Note that the projection can be regarded as a pattern correlation, where the patterns in Figure 6 are established by dynamical adjustment mechanisms and pathways (sections 3.2 and 3.3). We highlight three cases (Figures 6c and 6d) resulting from the pointwise projection in Equation 12:

(+) overlapping sensitivities of equal sign, resulting in a *positive* contribution to $\mathbf{q} \bullet \mathbf{v}^A$;
(−) overlapping sensitivities of opposite sign, resulting in a *negative* contribution to $\mathbf{q} \bullet \mathbf{v}^A$;
(0) nonoverlapping sensitivities, resulting in *no* contribution to $\mathbf{q} \bullet \mathbf{v}^A$.

Figure 7i is a quantitative summary of Figure 6, showing total positive (case (+)) and negative (case (−)) contributions to the projection $\mathbf{q} \bullet \mathbf{v}^A$, for the four different forcings. The maximum absolute value for the projection is equal to 1, due to normalization by $\sigma_{\mathrm{HT}}, \sigma_\star$ (Equation 12).

For all observations considered, the generation of proxy potential is dominated by existence of wind-driven adjustments that are shared with those for $\mathrm{HT}_{\mathrm{ISR}}$ (Figures 7i–7k). Minor importance of $Q_{\mathrm{net},\uparrow}$ and *EPR* is not surprising when recalling the fact that $\mathrm{HT}_{\mathrm{ISR}}$ is relatively insensitive to $Q_{\mathrm{net},\uparrow}$ and *EPR* (Figure 7a). Note that even for the surface temperature observation θ^C, which is highly sensitive to surface heat fluxes (Figure 7d), the $Q_{\mathrm{net},\uparrow}$ contribution to the projection in Equation 12 is negligible (Figure 7k).

Positive τ_y contributions to $\mathbf{q} \bullet \mathbf{v}^A$ arise along the eastern boundary of the subtropical North Atlantic (solid box, Figure 7f), where both $\mathrm{HT}_{\mathrm{ISR}}$ and θ^A exhibit a band of positive sensitivity along the western African and European coast (Figures 7e and 7f), due to the shared pressure adjustment mechanism discussed in sections 3.2 and 3.3 and Figures 5a and 5c. Negative τ_y contributions to $\mathbf{q} \bullet \mathbf{v}^A$ arise in the northeast Atlantic (dashed box, Figure 7f), where wind stress sensitivities are of large amplitude and of opposite sign for $\mathrm{HT}_{\mathrm{ISR}}$ (Figure 7e) and θ^A (Figure 7f), as discussed in section 3.3 and Figure 5d. The negative projection in the northeast Atlantic exceeds the positive projection in the eastern Atlantic waveguide (Figure 7i). Total positive and negative contributions sum to $\mathbf{q} \bullet \mathbf{v}^A = -0.44$ (Figure 7i). Here, partial cancellation between the positive and negative projections leads to a value reduced by $c^A = 0.29$. For $\star = A,B,C$, cancellation is quantified as

$$c^\star = |\mathbf{q}| \bullet |\mathbf{v}^\star| - |\mathbf{q} \bullet \mathbf{v}^\star| \geq 0 \tag{13}$$

where $|\mathbf{w}|$ denotes the vector whose entries are the absolute values of the respective entries of the vector $\mathbf{w}$, for $\mathbf{w} = \mathbf{q}, \mathbf{v}^\star$. As an example, if all contributions shown in Figure 7i were either consistently positive or consistently negative (in which cases no cancellation occurred), the absolute value of the projection $\mathbf{q} \bullet \mathbf{v}^A$ would be increased by the addition of c^A, resulting in an absolute value of $0.44 + 0.29 = 0.73$.

Positive wind stress contributions to $\mathbf{q} \bullet \mathbf{v}^B$ (Figure 7j) are of similar magnitude as positive wind stress contributions to $\mathbf{q} \bullet \mathbf{v}^A$ (Figure 7i), due to the pressure adjustment mechanism in the eastern Atlantic waveguide, shared among θ^B, $\mathrm{HT}_{\mathrm{ISR}}$ (and θ^A). The total overlap of $\mathrm{HT}_{\mathrm{ISR}}$ sensitivity with θ^B sensitivity (Figure 7j) is much smaller than with θ^A sensitivity (Figure 7i), since θ^B does not show any sensitivity north of 55° (Figure 7g). For the Irminger Sea surface observation θ^C, proxy origins are similar as for the Irminger Sea subsurface observation θ^A (boxes in Figures 7f and 7h), but contributions from each forcing are reduced by a factor of about 0.25 (Figures 7i ans 7k), due to relatively weaker excitation of surface temperature by remote forcing, as discussed in section 3.3.

The DPP (Equation 4) of $\theta^\star$ for $\mathrm{HT}_{\mathrm{ISR}}$ is given by $\mathbf{q} \bullet \mathbf{v}^\star$ squared. The result is shown in Figures 7l–7n: The DPP of θ^A for $\mathrm{HT}_{\mathrm{ISR}}$ is 19%, while the DPPs of θ^B and θ^C for $\mathrm{HT}_{\mathrm{ISR}}$ are only 1%. These values can be interpreted either in terms of (i) shared ocean adjustment physics or (ii) uncertainty quantification (cf. Figure 1c). As for (i), $\mathrm{HT}_{\mathrm{ISR}}$ shares 19% of its dynamical causes with θ^A, but only 1% with θ^B and θ^C. As a result, θ^A (θ^B, θ^C) captures 19% (1%, 1%) of the variability of $\mathrm{HT}_{\mathrm{ISR}}$, taking into account all potential forcing scenarios. As for (ii), DPP predicts that uncertainty in $\mathrm{HT}_{\mathrm{ISR}}$ would get reduced by 19% (1%, 1%), if a noise-free measurement value of θ^A (θ^B, θ^C) was added to the state estimation framework that was described in section 3.1.

4. Discussion

The design of effective climate observing systems relies on a both *physical* and *quantitative* understanding of which QoIs that capture important aspects of the climate system can be informed by existing or future

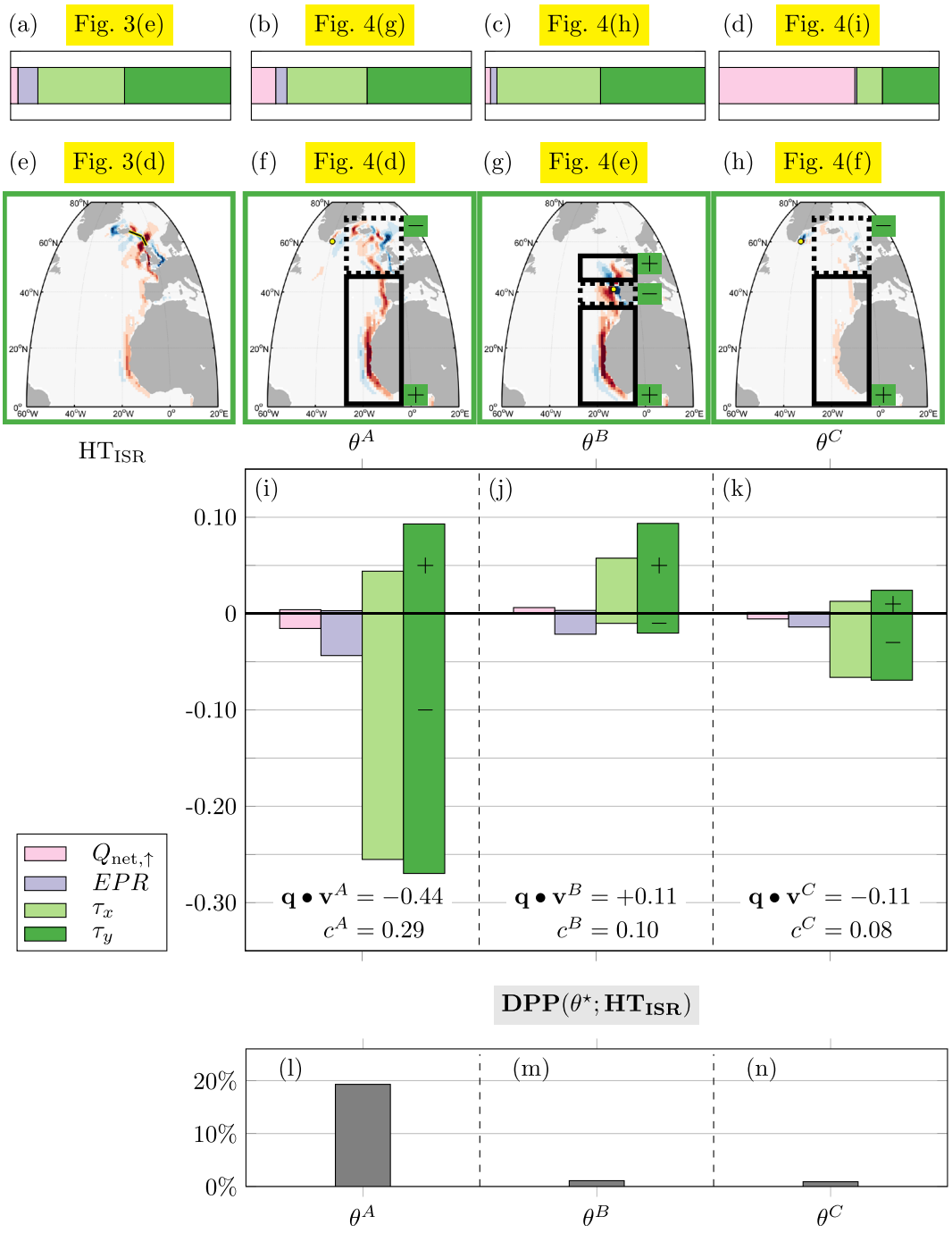

Figure 7. (a–h) Replots of subpanels in Figures 3 and 4, as indicated by the yellow labels. (i–k) Contributions from the forcings $F_m = Q_{\mathrm{net},\uparrow}, EPR, \tau_x, \tau_y$ to the projection $\mathbf{q} \bullet \mathbf{v}^\star$ (Equation 12), where (i) $\star = A$, (j) $\star = B$, and (k) $\star = C$. The projections are computed as shown in Figure 6. That is, in each of the subpanels (i–k), the τ_y contribution is computed by projecting the sensitivity map $\sigma_{\mathrm{HT}}^{-1} \frac{\partial(\mathrm{HT_{ISR}})}{\partial \tau_y(i,j)} \Delta\tau_y$ (shown in (e)) onto the respective sensitivity map $\sigma_\star^{-1} \frac{\partial \theta^\star}{\partial \tau_y(i,j)} \Delta\tau_y$ (shown in (f) for $\star = A$, (g) for $\star = B$, and (h) for $\star = C$). Positive (negative) τ_y contributions arise in the Atlantic subregion inside the black solid (dashed) box in (f) for $\star = A$, (g) for $\star = B$, and (h) for $\star = C$, inside which sensitivities correlate (anticorrelate) with those in panel (e). The value for $\mathbf{q} \bullet \mathbf{v}^\star$ (bottom of panels (i)–(k)) is obtained by summing up all upward and downward pointing bars in the respective subpanel. Here, destructive interference is quantified by $c^\star$ (Equation 13). (l–n) Dynamical proxy potential of (l) θ^A, (m) θ^B, and (n) θ^C for $\mathrm{HT_{ISR}}$, computed by $\mathrm{DPP}(\theta^\star;\ \mathrm{HT_{ISR}}) = (\mathbf{q} \bullet \mathbf{v}^\star)^2$ (see Equation 4).

observations. Toward this goal, we introduced the concept of DPP by establishing a parallel between (i) ocean dynamical principles and (ii) Hessian uncertainty quantification (UQ). Hessian UQ is currently being explored in the computational sciences as a tool for optimal observing system design (Alexanderian et al., 2016; Bui-Thanh et al., 2012, 2013; Flath et al., 2011; Isaac et al., 2015) but has so far not been applied in the context of global ocean state estimation. With its two interpretations, DPP provides a means to optimally design climate observing systems, while giving insight into the governing physical mechanisms.

In the following, we summarize the results from our North Atlantic case study (section 4.1), discuss our method in the context of related work in oceanography (section 4.2), point out limitations (section 4.3), and provide directions for future work (section 4.4).

4.1. Summary of Shared Pathways

On a 5 year time scale, our example QoI, heat transport across the ISR (HT_{ISR}), and the examined Irminger Sea subsurface temperature observation, θ^A, are most sensitive to changes in wind forcing in two main regions: (I) along the eastern boundary of the subtropical North Atlantic and (II) in the northeast Atlantic and the Nordic Seas. Wind forcing in Region (I) excites a pressure adjustment mechanism, which strengthens (or weakens) both the ISR geostrophic transport and the IC, leading to anomalies in HT_{ISR} and θ^A of equal sign. Wind forcing in Region (II) drives an anomalous barotropic circulation around Iceland which simultaneously strengthens (or weakens) the Norwegian Atlantic and East Greenland Currents, leading to anomalies in θ^A and HT_{ISR} of opposite sign.

DPP measures the degree of shared adjustment physics between the QoI and observation under consideration, taking into account the effects of constructive and destructive interference of information propagation (Figure 7). Destructive interference of information occurs because wind forcing in Region (I) leads to responses in HT_{ISR} and θ^A of equal sign, while wind forcing in Region (II) leads to responses in HT_{ISR} and θ^A of opposite sign. Considering the 5 year mean of the two quantities, we find that the DPP of θ^A for HT_{ISR} is 19%. DPP allows two equivalent interpretations: θ^A (i) shares 19% of its adjustment physics with HT_{ISR}; (ii) reduces the uncertainty in HT_{ISR} by 19%, if θ^A is added without noise to the ECCO state estimate.

4.2. Relation to Previous Work

Complete sensitivity information, enabled by the adjoint of an ocean GCM, is the cornerstone of quantifying DPP. In previous work, adjoint-derived sensitivity information has been proposed to support observing system design in a distinct fashion: Marotzke et al. (1999), Köhl and Stammer (2004), and Heimbach et al. (2011) suggest that regions in which a given QoI shows highest sensitivity to hydrographic state variables are to be prioritized when deploying new hydrographic observations. The philosophy of these studies is to discover direct cause and effect relationships between changes in observations and changes in the QoI. DPP looks further: by employing sensitivity information of not only the QoI but also of the observations, DPP quantifies dynamics-based covariability of the QoI and observations, driven by local or remote forcings. As a result, DPP can exploit that multiple distinct QoIs may be connected by basin-wide dynamical adjustments and thus well constrained by limited instrumentation in this shared adjustment pathway. Moreover, unlike DPP, the adjoint-based studies referenced above do not provide a *quantitative* estimate on how well the QoI is constrained by the suggested observations (and how much information is missing). Instead, the previous studies provide only a relative estimate by suggesting that some observations may be more informative than others.

A similar description to DPP can be obtained through the method of representers (Bennett, 1985, 2002; see also our section 2). In the context of variational data assimilation, a representer assesses the impact of an assimilated observation on the estimated model state (e.g., Bennett, 1985, 1990; Kurapov et al., 2009). Representer-based methods have been used to evaluate observing systems and strategies in regional settings on short (daily to weekly) time scales (e.g., Moore et al., 2017; Zhang et al., 2010). DPP, as introduced in this work, views representers from a new perspective, with the merit to highlight the important role of dynamical pathways and adjustment processes (Figures 6and 7) in establishing and quantifying the information content of an observation for a QoI. Moreover, DPP operates—for the first time—within global ocean state estimation, focusing on climate observing systems, longer (monthly to multiannual) time scales, and large-scale ocean circulation.

In the context of Arctic observing system design, Kaminski et al. (2015, 2018) utilized a method related to DPP. A key difference is that the authors handle sensitivity information averaged over large regions (e.g., Figure 2 in Kaminski et al., 2015). While spatially averaged sensitivity enables numerically efficient quantification of the constraint from large-scale data acquisitions (e.g., from satellite or aircraft), it could entail large aggregation errors (Kaminski et al., 2001). Furthermore, we argue that it inhibits clear understanding of proxy origins, by grouping information from dynamically distinct regions. This is especially true for harnessing proxy potential from shared wind-driven adjustments, for which resolution of the coastal wave guides is key.

4.3. Limitations

While the adjoint model provides comprehensive sensitivity information throughout the entire model space-time domain, adjoint-derived sensitivity is limited by the linear approximation and inexactness of the adjoint (Czeschel et al., 2010; Errico, 1997; Hoteit et al., 2005). Nevertheless, perturbation experiments with the full nonlinear model dynamics in Appendix A show that the adjoint-derived sensitivities in our case study reliably capture the basin-wide adjustment mechanisms that are excited by wind stress perturbations in Regions (I) and (II). However, estimation errors in the predicted response amplitudes can reach up to 20%—partly due to the linear approximation, and partly due to the inexactness of the adjoint. This emphasizes that we must keep validating the accuracy of adjoint-derived sensitivity information and that improving the exactness of the adjoint would add great value to dynamics-based observing system design.

A second shortcoming of the methodology presented here is that DPP may be dependent on the underlying ocean GCM. Global ocean GCMs are typically too coarse (here: nominally 1° horizontal resolution) to accurately represent important processes including density-driven gravity currents (e.g., across overflow regions in the subpolar North Atlantic), deep convection, and narrow boundary currents. Inability to test model dependency, due to unavailable adjoints for almost all GCMs, is a limiting factor.

As a third drawback, important limiting assumptions entering the calculation of DPP are the choice of control variables and associated prior covariance (or weights). The control variables should include all uncertain elements in the model, that is, the parts that are not determined by the known governing equations (Figure 1c). The associated weights reflect prior uncertainties in the control variables. In the choice of uncertain control variables and weights, DPP follows the assumptions of ocean state estimation (while in our case study, we simplified controls and weights, for the sake of adding clarity to our presentation, see section 3.1.2). It is important to note that, while the sensitivities, utilized for the computation of DPP, uncover all dynamical adjustment processes (independent of the weights), the relative importance of these mechanisms is determined by the weights.

4.4. Future Directions

In our case study, we investigated how changes in time-mean forcing affect the time means of temperature observations and QoI, on 5 year time scales. Thereby, we identified key forcings, adjustment pathways, and mechanisms for observations and QoI, but did not disentangle whether the dominating mechanisms operate on monthly, annual, or multiannual (<5 years) time scales. Future work should consider time-variable changes in forcing and investigate the variability of observations and QoIs on shorter (e.g., interannual) time scales. A further important extension of the work presented here is to account for observational noise as well as data redundancy and complementarity between multiple observations. This objective will be pursued in a forthcoming paper.

5. Conclusions

The oceanographic community would strongly benefit from a synergistic, quantitative approach to codesign a cost-effective, long-term, and sustained ocean observing system (National Academies of Sciences, 2017). Motivated by this objective, we have introduced the concept of DPP, a dynamics-based alternative to statistical correlation analysis and conventional observing system simulation experiments (OSSEs). Our main conclusions are the following.

(1) In contrast to statistical proxy potential, DPP only accounts for covariability that has a dynamical underpinning, by tracing variability back to common causal forcings. Wind-driven adjustment

mechanisms along the ocean boundaries, similar to the ones identified in this study (section 4.1), have been shown to be key for many distinct oceanic quantities (Fukumori et al., 2007, 2015; Heimbach et al., 2011; Jones et al., 2018; Marotzke et al., 1999; Pillar et al., 2016; Smith & Heimbach, 2019). By identifying these common dynamical pathways and mechanisms via DPP assessment, we elucidate the *physical cause of observed covariability* in the North Atlantic.

(2) Our method accounts for all dynamically feasible pathways between observation and QoI, and with the potential for constructive and destructive interference of information propagation. Unraveling constructive and destructive contributions to DPP, as performed here, paves the way for extracting *complementary information* from observations. By targeting information that is complementary to existing observing systems, the notion of DPP can support the design of efficient and effective future observing systems.

(3) In order to evaluate DPP, one does not require actual observational data, since DPP investigates the dynamical relationships between observation and QoI in the model. DPP gains its full power for *observing system design* through the following fact. Independent of the measurement value (potentially taken by a future observing system), inclusion of the observation in the underlying state estimation framework will reduce uncertainty in the QoI by the predetermined value of DPP.

(4) Based on endpoint geostrophy, moorings that are to be informative for cross-section transports would be located along the section itself. Here, we demonstrated that *remote* hydrographic *observations can provide strong constraints* on cross-section transports due to large-scale oceanic teleconnections. This result highlights the importance of further probing the dynamical constraints contained within the existing observational database.

Finally, the fact that the efficiency of observing systems depends on the targeted QoIs highlights the importance of an ongoing community discussion on which climate QoIs are most important to constrain.

Appendix A: Linear Approximation and Inexactness of the Adjoint

The adjoint of an ocean GCM provides comprehensive sensitivity information, which is the key ingredient of DPP (Equation 4). Caveats are that (i) adjoint-derived sensitivities provide only a linear approximation and that (ii) the adjoint may be inexact, for example, due to artificially increased viscosity compared to the forward model, which is often a requirement to stabilize the adjoint (Forget et al., 2015; Hoteit et al., 2005, 2010). Here, we verify adjoint-derived sensitivities against perturbation experiments with the nonlinear forward model. Our control simulation covers the final 5 years of the ECCOv4r2 state estimate. We focus on meridional wind stress perturbations inside the two green regions in Figure 5, along the western African coast and the western Icelandic coast.

For each of the two chosen regions, we perform two separate perturbation experiments, imposing meridional wind stress anomalies of $\Delta\tau_y = \pm 0.05\ \mathrm{N/m^2}$ inside the region, respectively. We maintain the wind stress perturbation over the full 5 year period. For $J \in \{\theta^A,\ \theta^B,\ \mathrm{HT_{ISR}}\}$ (Equations 6 and 7), we then compute the differences

$$\Delta^{\pm}_{\mathrm{fwd}} J = J^{\pm} - J^{0}. \tag{A1}$$

Here, J^0 denotes the quantity J in the control simulation, and J^+ and J^- the same quantity in the simulation with the positive and negative perturbation, respectively. $\Delta^{+}_{\mathrm{fwd}} J$ and $-\Delta^{-}_{\mathrm{fwd}} J$ are identical if J depends linearly on τ_y inside the chosen perturbation region. Even if a resemblance of $\Delta^{+}_{\mathrm{fwd}} J$ and $-\Delta^{-}_{\mathrm{fwd}} J$ suggests a linear response, the adjoint-derived anomalies can still deviate from the forward anomalies, due to inexactness of the adjoint. Therefore, we next compare the forward anomalies $\Delta^{+}_{\mathrm{fwd}} J$ and $-\Delta^{-}_{\mathrm{fwd}} J$ to the adjoint estimate

$$\Delta^{+}_{\mathrm{adj}} J = \frac{\partial J}{\partial \tau_y} \cdot \Delta\tau_y, \tag{A2}$$

where $\Delta\tau_y$ now denotes the positive meridional wind stress anomaly ($+0.05\ \mathrm{N/m^2}$) inside the chosen region.

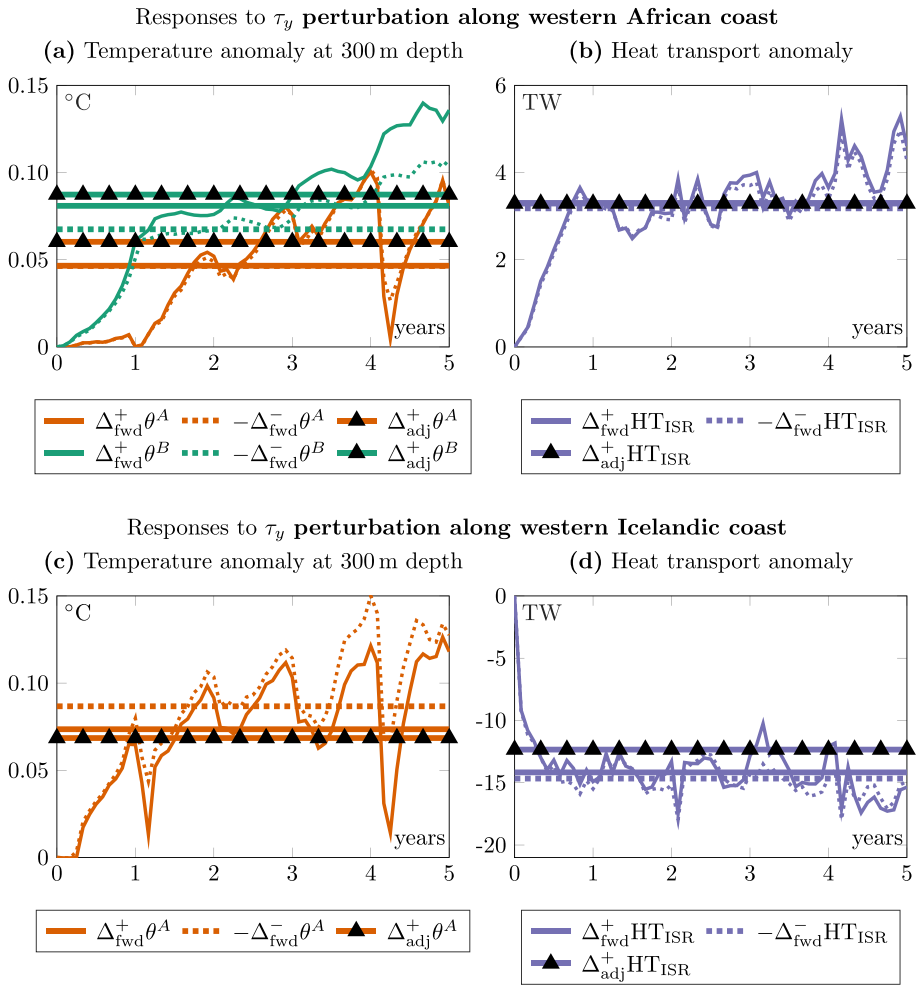

Figure A1. Anomalies in (a and c) $J=\theta^A,\theta^B$ and (b and d) $J=\text{HT}_{\text{ISR}}$, in response to meridional wind stress (τ_y) perturbations along the (a and b) western African coast and (c and d) western Icelandic coast. The solid versus dashed, thick, horizontal lines show the 5 year mean of the anomalies $\Delta^+_{\text{fwd}}J$ versus $-\Delta^-_{\text{fwd}}J$ (Equation A1), diagnosed from the nonlinear forward perturbation experiments. The corresponding thin lines present the monthly evolution of $\Delta^+_{\text{fwd}}J$ versus $-\Delta^-_{\text{fwd}}J$, as a function of years since the start of the perturbation. The thick, horizontal lines with black triangles show the adjoint-derived (5 year mean) anomalies $\Delta^+_{\text{adj}}J$ (Equation A2). In (c), the response anomaly in θ^B is invisible because it is 2 orders of magnitude smaller than the response anomaly in θ^A.

In Figure A1, we see notable deviations between $\Delta^+_{\text{fwd}}J$ and $-\Delta^-_{\text{fwd}}J$ in two cases: for the anomalies in $J=\theta^B$ in response to a τ_y perturbation along the western African coast (green solid vs. dashed horizontal lines, Figure A1a), and for the anomaly in $J=\theta^A$ in response to a τ_y perturbation along the western Icelandic coast (orange solid vs. dashed horizontal lines, Figure A1c). In both cases, the amplitudes of the time-evolving forward anomalies start to develop an offset after 1–2 years. Since anomalies in θ^A and θ^B are the time-integrated result of ocean transport anomalies, the offset tends to becomes larger over time. In contrast, $\Delta^+_{\text{fwd}}\text{HT}_{\text{ISR}}$ and $-\Delta^-_{\text{fwd}}\text{HT}_{\text{ISR}}$ coincide (Figures A1b and A1d), suggesting that HT_{ISR} is linear as a function of τ_y in the tested perturbation regions. Note, however, that, despite the suggested linearity, $\Delta^+_{\text{adj}}\text{HT}_{\text{ISR}}$ slightly differs from the forward anomalies in Figure A1d, due to an inexact adjoint. A similar situation occurs in Figure A1a for the response anomalies in θ^A. In all cases shown in Figure A1, the adjoint estimate $\Delta^+_{\text{adj}}J$ predicts the response anomalies in J with the correct sign. Moreover, predicted amplitudes are generally close to those of the forward anomalies, although, in few cases, they can be off by up to 20%.

Acknowledgments

N. L. and K. H. N. were supported by the ice2ice project funded by the European Research Council under the European Community Seventh Framework Programme (FP7/2007-2013)/ERC Grant Agreement 610055. P. H. and H. R. P. received funding in part from the NSF Grant NSF-OCE-1924546 and the Estimating the Circulation and Climate of the Ocean (ECCO) project via a JPL/Caltech subcontract. The ECCOv4r2 model setup used in this work can be accessed from public repositories and permanent archives (Campin et al., 2019; Forget, 2018, 2016a, 2016b). Adjoint code was generated using the TAF software tool, created and maintained by FastOpt GmbH (http://www.fastopt.com/). We thank two anonymous reviewers for comments that greatly improved the manuscript. We wish to thank Céline Heuzé, Andrew Moore, Timothy Smith, Gael Forget, Carl Wunsch, and Daniel Jones for helpful discussions.

References

Alexander-Turner, R., Ortega, P., & Robson, J. I. (2018). How robust are the surface temperature fingerprints of the Atlantic Overturning Meridional Circulation on monthly time scales? *Geophysical Research Letters*, *45*, 3559–3567. https://doi.org/10.1029/2017GL076759

Alexanderian, A., Petra, N., Stadler, G., & Ghattas, O. (2016). A fast and scalable method for a-optimal design of experiments for infinite-dimensional Bayesian nonlinear inverse problems. *SIAM Journal on Scientific Computing*, *38*(1), A243–A272. https://doi.org/10.1137/140992564

Årthun, M., & Eldevik, T. (2016). On anomalous ocean heat transport toward the Arctic and associated climate predictability. *Journal of Climate*, *29*(2), 689–704. https://doi.org/10.1175/JCLI-D-15-0448.1

Asbjørnsen, H., Årthun, M., Skagseth, O., & Eldevik, T. (2019). Mechanisms of ocean heat anomalies in the Norwegian Sea. *Journal of Geophysical Research: Oceans*, *124*, 2908–2923. https://doi.org/10.1029/2018JC014649

Baehr, J., Haak, H., Alderson, S., Cunningham, S. A., Jungclaus, J. H., & Marotzke, J. (2007). Timely detection of changes in the Meridional Overturning Circulation at 26°N in the Atlantic. *Journal of Climate*, *20*(23), 5827–5841. https://doi.org/10.1175/2007JCLI1686.1

Bennett, A. F. (1985). Array design by inverse methods. *Progress in Oceanography*, *15*(2), 129–156. https://doi.org/10.1016/0079-6611(85)90033-3

Bennett, A. F. (1990). Inverse methods for assessing ship-of-opportunity networks and estimating circulation and winds from tropical expendable bathythermograph data. *Journal of Geophysical Research*, *95*(C9), 16,111–16,148. https://doi.org/10.1029/JC095iC09p16111

Bennett, A. F. (2002). *Inverse modeling of the ocean and atmosphere*. Cambridge: Cambridge University Press. https://doi.org/10.1017/CBO9780511535895

Berx, B., Hansen, B., Østerhus, S., Larsen, K. M., Sherwin, T., & Jochumsen, K. (2013). Combining in situ measurements and altimetry to estimate volume, heat and salt transport variability through the Faroe-Shetland Channel. *Ocean Science*, *9*(4), 639–654. https://doi.org/10.5194/os-9-639-2013

Bingham, R. J., & Hughes, C. W. (2009). Signature of the Atlantic meridional overturning circulation in sea level along the east coast of North America. *Geophysical Research Letters*, *36*, L02603. https://doi.org/10.1029/2008GL036215

Buckley, M. W., Ponte, R. M., Forget, G., & Heimbach, P. (2014). Low-frequency SST and upper-ocean heat content variability in the North Atlantic. *Journal of Climate*, *27*(13), 4996–5018. https://doi.org/10.1175/JCLI-D-13-00316.1

Bui-Thanh, T., Burstedde, C., Ghattas, O., Martin, J., Stadler, G., & Wilcox, L. C. (2012). Extreme-scale UQ for Bayesian inverse problems governed by PDEs. In *SC '12: Proceedings of the international conference on high performance computing, networking, storage and analysis* (pp. 1–11). Salt Lake City, UT. https://doi.org/10.1109/SC.2012.56

Bui-Thanh, T., Ghattas, O., Martin, J., & Stadler, G. (2013). A computational framework for infinite-dimensional Bayesian inverse problems Part I: The linearized case, with application to global seismic inversion. *SIAM Journal on Scientific Computing*, *35*(6), A2494–A2523. https://doi.org/10.1137/12089586X

Caesar, L., Rahmstorf, S., Robinson, A., Feulner, G., & Saba, V. (2018). Observed fingerprint of a weakening Atlantic Ocean overturning circulation. *Nature*, *556*(7700), 191–196. https://doi.org/10.1038/s41586-018-0006-5

Campin, J.-M., Heimbach, P., Losch, M., Forget, G., Hill, E., Adcroft, A., et al. (2019). MITgcm/MITgcm: Checkpoint67m. Zenodo.

Chaudhuri, A. H., Ponte, R. M., Forget, G., & Heimbach, P. (2013). A comparison of atmospheric reanalysis surface products over the ocean and implications for uncertainties in air-sea boundary forcing. *Journal of Climate*, *26*(1), 153–170. https://doi.org/10.1175/JCLI-D-12-00090.1

Czeschel, L., Marshall, D. P., & Johnson, H. L. (2010). Oscillatory sensitivity of Atlantic overturning to high-latitude forcing. *Geophysical Research Letters*, *37*, L10601. https://doi.org/10.1029/2010GL043177

Errico, R. M. (1997). What is an adjoint model? *Bulletin of the American Meteorological Society*, *78*(11), 2577–2591. https://doi.org/10.1175/1520-0477(1997)078<2577:WIAAM>2.0.CO;2

Ezer, T. (2015). Detecting changes in the transport of the Gulf Stream and the Atlantic overturning circulation from coastal sea level data: The extreme decline in 2009–2010 and estimated variations for 1935–2012. *Global and Planetary Change*, *129*, 23–36. https://doi.org/10.1016/j.gloplacha.2015.03.002

Flath, H., Wilcox, L., Akçelik, V., Hill, J., van Bloemen Waanders, B., & Ghattas, O. (2011). Fast algorithms for Bayesian uncertainty quantification in large-scale linear inverse problems based on low-rank partial Hessian approximations. *SIAM Journal on Scientific Computing*, *33*(1), 407–432. https://doi.org/10.1137/090780717

Forget, G. (2016a). ECCO version 4 release 2 inputs: Model initialization. Harvard Dataverse.

Forget, G. (2016b). ECCO version 4 release 2 inputs: Surface forcing fields. Harvard Dataverse.

Forget, G. (2018). Gaelforget/eccov4: Documentation updates. Zenodo.

Forget, G., Campin, J.-M., Heimbach, P., Hill, C. N., Ponte, R. M., & Wunsch, C. (2015). ECCO version 4: An integrated framework for non-linear inverse modeling and global ocean state estimation. *Geoscientific Model Development*, *8*(10), 3071–3104. https://doi.org/10.5194/gmd-8-3071-2015

Frajka-Williams, E. (2015). Estimating the Atlantic overturning at 26°N using satellite altimetry and cable measurements. *Geophysical Research Letters*, *42*, 3458–3464. https://doi.org/10.1002/2015GL063220

Frajka-Williams, E., Ansorge, I. J., Baehr, J., Bryden, H. L., Chidichimo, M. P., Cunningham, S. A., et al. (2019). Atlantic Meridional Overturning Circulation: Observed transport and variability. *Frontiers in Marine Science*, *6*, 260. https://doi.org/10.3389/fmars.2019.00260

Fu, L.-L., Lee, T., Liu, W. T., & Kwok, R. (2018). 50 Years of satellite remote sensing of the ocean. *Meteorological Monographs*, *59*, 5.1–5.46. Publisher: American Meteorological Society. https://doi.org/10.1175/AMSMONOGRAPHS-D-18-0010.1

Fukumori, I., Menemenlis, D., & Lee, T. (2007). A near-uniform basin-wide sea level fluctuation of the Mediterranean Sea. *Journal of Physical Oceanography*, *37*(2), 338–358. https://doi.org/10.1175/JPO3016.1

Fukumori, I., Wang, O., Llovel, W., Fenty, I., & Forget, G. (2015). A near-uniform fluctuation of ocean bottom pressure and sea level across the deep ocean basins of the Arctic Ocean and the Nordic Seas. *Progress in Oceanography*, *134*, 152–172. https://doi.org/10.1016/j.pocean.2015.01.013

Galanti, E., & Tziperman, E. (2003). A midlatitude-ENSO teleconnection mechanism via baroclinically unstable long Rossby waves. *Journal of Physical Oceanography*, *33*(9), 1877–1888. https://doi.org/10.1175/1520-0485(2003)033<1877:AMTMVB>2.0.CO;2

Galanti, E., Tziperman, E., Harrison, M., Rosati, A., Giering, R., & Sirkes, Z. (2002). The equatorial thermocline outcropping—A seasonal control on the Tropical Pacific Ocean-atmosphere instability strength. *Journal of Climate*, *15*(19), 2721–2739. https://doi.org/10.1175/1520-0442(2002)015<2721:TETOAS>2.0.CO;2

Giering, R., & Kaminski, T. (1998). Recipes for adjoint code construction. *ACM Transactions on Mathematical Software*, *24*(4), 437–474.

Hansen, B., Larsen, K. M. H., Hátún, H., Kristiansen, R., & Mortensen, S. (2015). Transport of volume, heat, and salt towards the Arctic in the Faroe Current 1993-2013. *Ocean Science*, *11*(5), 743–757. https://doi.org/10.5194/os-11-743-2015

Hansen, B., & Østerhus, S. (2000). North Atlantic–Nordic Seas exchanges. *Progress in Oceanography*, *45*(2), 109–208. https://doi.org/10.1016/S0079-6611(99)00052-X

Hansen, B., Østerhus, S., Hátún, H., Kristiansen, R., & Larsen, K. M. H. (2003). The Iceland-Faroe inflow of Atlantic water to the Nordic Seas. *Progress in Oceanography*, *59*(4), 443–474. https://doi.org/10.1016/j.pocean.2003.10.003

Heimbach, P., Wunsch, C., Ponte, R. M., Forget, G., Hill, C., & Utke, J. (2011). Timescales and regions of the sensitivity of Atlantic meridional volume and heat transport: Toward observing system design. *Deep Sea Research Part II: Topical Studies in Oceanography*, *58*(17-18), 1858–1879. https://doi.org/10.1016/j.dsr2.2010.10.065

Hoteit, I., Cornuelle, B., & Heimbach, P. (2010). An eddy-permitting, dynamically consistent adjoint-based assimilation system for the tropical Pacific: Hindcast experiments in 2000. *Journal of Geophysical Research*, *115*, C03001. https://doi.org/10.1029/2009JC005437

Hoteit, I., Cornuelle, B., Köhl, A., & Stammer, D. (2005). Treating strong adjoint sensitivities in tropical eddy-permitting variational data assimilation. *Quarterly Journal of the Royal Meteorological Society*, *131*(613), 3659–3682. https://doi.org/10.1256/qj.05.97

Isaac, T., Petra, N., Stadler, G., & Ghattas, O. (2015). Scalable and efficient algorithms for the propagation of uncertainty from data through inference to prediction for large-scale problems, with application to flow of the Antarctic ice sheet. *Journal of Computational Physics*, *296*, 348–368. https://doi.org/10.1016/j.jcp.2015.04.047

Jones, D., Forget, G., Sinha, B., Josey, S., Boland, E., Meijers, A., & Shuckburgh, E. (2018). Local and remote influences on the heat content of the Labrador Sea: An adjoint sensitivity study. *Journal of Geophysical Research: Oceans*, *123*, 2646–2667. https://doi.org/10.1002/2018JC013774

Kaminski, T., Kauker, F., Eicken, H., & Karcher, M. (2015). Exploring the utility of quantitative network design in evaluating Arctic sea ice thickness sampling strategies. *The Cryosphere*, *9*(4), 1721–1733. https://doi.org/10.5194/tc-9-1721-2015

Kaminski, T., Kauker, F., Toudal Pedersen, L., Voßbeck, M., Haak, H., Niederdrenk, L., et al. (2018). Arctic Mission Benefit Analysis: Impact of sea ice thickness, freeboard, and snow depth products on sea ice forecast performance. *The Cryosphere*, *12*(8), 2569–2594. https://doi.org/10.5194/tc-12-2569-2018

Kaminski, T., Rayner, P. J., Heimann, M., & Enting, I. G. (2001). On aggregation errors in atmospheric transport inversions. *Journal of Geophysical Research*, *106*(D5), 4703–4715. https://doi.org/10.1029/2000JD900581

Knight, J. R., Allan, R. J., Folland, C. K., Vellinga, M., & Mann, M. E. (2005). A signature of persistent natural thermohaline circulation cycles in observed climate. *Geophysical Research Letters*, *32*, L20708. https://doi.org/10.1029/2005GL024233

Köhl, A. (2005). Anomalies of Meridional Overturning: Mechanisms in the North Atlantic. *Journal of Physical Oceanography*, *35*(8), 1455–1472. https://doi.org/10.1175/JPO2767.1

Köhl, A., & Stammer, D. (2004). Optimal observations for variational data assimilation. *Journal of Physical Oceanography*, *34*(3), 529–542. https://doi.org/10.1175/2513.1

Kurapov, A. L., Egbert, G. D., Allen, J. S., & Miller, R. N. (2009). Representer-based analyses in the coastal upwelling system. *Dynamics of Atmospheres and Oceans*, *48*(1), 198–218. https://doi.org/10.1016/j.dynatmoce.2008.09.002

Landerer, F. W., Wiese, D. N., Bentel, K., Boening, C., & Watkins, M. M. (2015). North Atlantic meridional overturning circulation variations from GRACE ocean bottom pressure anomalies. *Geophysical Research Letters*, *42*, 8114–8121. https://doi.org/10.1002/2015GL065730

Latif, M., Roeckner, E., Botzet, M., Esch, M., Haak, H., Hagemann, S., et al. (2004). Reconstructing, monitoring, and predicting multidecadal-scale changes in the North Atlantic thermohaline circulation with sea surface temperature. *Journal of Climate*, *17*(7), 1605–1614. https://doi.org/10.1175/1520-0442(2004)017<1605:RMAPMC>2.0.CO;2

Lherminier, P., Mercier, H., Gourcuff, C., Alvarez, M., Bacon, S., & Kermabon, C. (2007). Transports across the 2002 Greenland-Portugal Ovide section and comparison with 1997. *Journal of Geophysical Research*, *112*, C07003. https://doi.org/10.1029/2006JC003716

Little, C. M., Hu, A., Hughes, C. W., McCarthy, G. D., Piecuch, C. G., Ponte, R. M., & Thomas, M. D. (2019). The relationship between U.S. East Coast sea level and the Atlantic Meridional Overturning Circulation: A review. *Journal of Geophysical Research: Oceans*, *124*, 6435–6458. https://doi.org/10.1029/2019JC015152

Lopez, H., Goni, G., & Dong, S. (2017). A reconstructed South Atlantic Meridional Overturning Circulation time series since 1870. *Geophysical Research Letters*, *44*, 3309–3318. https://doi.org/10.1002/2017GL073227

Lozier, M. S., Bacon, S., Bower, A. S., Cunningham, S. A., Femke de Jong, M., de Steur, L., et al. (2017). Overturning in the Subpolar North Atlantic Program: A new international ocean observing system. *Bulletin of the American Meteorological Society*, *98*(4), 737–752. https://doi.org/10.1175/BAMS-D-16-0057.1

Lozier, M. S., Li, F., Bacon, S., Bahr, F., Bower, A. S., Cunningham, S. A., et al. (2019). A sea change in our view of overturning in the subpolar North Atlantic. *Science*, *363*(6426), 516–521. https://doi.org/10.1126/science.aau6592

Marotzke, J., Giering, R., Zhang, K. Q., Stammer, D., Hill, C., & Lee, T. (1999). Construction of the adjoint MIT ocean general circulation model and application to Atlantic heat transport sensitivity. *Journal of Geophysical Research*, *104*(C12), 29,529–29,547.

Marshall, J., Adcroft, A., Hill, C., Perelman, L., & Heisey, C. (1997). A finite-volume, incompressible Navier Stokes model for studies of the ocean on parallel computers. *Journal of Geophysical Research*, *102*(C3), 5753–5766. https://doi.org/10.1029/96JC02775

Marshall, J., Hill, C., Perelman, L., & Adcroft, A. (1997). Hydrostatic, quasi-hydrostatic, and nonhydrostatic ocean modeling. *Journal of Geophysical Research*, *102*(C3), 5733–5752. https://doi.org/10.1029/96JC02776

Marshall, D. P., & Johnson, H. L. (2013). Propagation of Meridional Circulation Anomalies along Western and Eastern Boundaries. *Journal of Physical Oceanography*, *43*(12), 2699–2717. https://doi.org/10.1175/JPO-D-13-0134.1

McCarthy, G. D., Brown, P. J., Flagg, C. N., Goni, G., Houpert, L., Hughes, C. W., et al. (2019). Sustainable observations of the AMOC: Methodology and technology. *Reviews of Geophysics*, *58*, e2019RG000654. https://doi.org/10.1038/nature14491

McCarthy, G. D., Haigh, I. D., Hirschi, J. J.-M., Grist, J. P., & Smeed, D. A. (2015). Ocean impact on decadal Atlantic climate variability revealed by sea-level observations. *Nature*, *521*(7553), 508–510. https://doi.org/10.1038/nature14491

Mercier, H., Lherminier, P., Sarafanov, A., Gaillard, F., Daniault, N., Desbruyères, D., et al. (2015). Variability of the meridional overturning circulation at the Greenland-Portugal OVIDE section from 1993 to 2010. *Progress in Oceanography*, *132*, 250–261. https://doi.org/10.1016/j.pocean.2013.11.001

Moore, A. M., Arango, H. G., & Edwards, C. A. (2017). Reduced-rank array modes of the California current observing system. *Journal of Geophysical Research: Oceans*, *123*, 452–465. https://doi.org/10.1002/2017JC013172

National Academies of Sciences, E. (2017). *Sustaining ocean observations to understand future changes in Earth's climate*. Washington, DC: The National Academies Press. https://doi.org/10.17226/24919

Orvik, K. A., & Skagseth, O. (2005). Heat flux variations in the eastern Norwegian Atlantic Current toward the Arctic from moored instruments, 1995–2005. *Geophysical Research Letters*, *32*, L14610. https://doi.org/10.1029/2005GL023487

Østerhus, S., Turrell, W. R., Jónsson, S., & Hansen, B. (2005). Measured volume, heat, and salt fluxes from the Atlantic to the Arctic Mediterranean. *Geophysical Research Letters*, *32*, L07603. https://doi.org/10.1029/2004GL022188

Østerhus, S., Woodgate, R., Valdimarsson, H., Turrell, B., Steur, L., Quadfasel, D., et al. (2019). Arctic Mediterranean exchanges: A consistent volume budget and trends in transports from two decades of observations. *Ocean Science*, *15*(2), 379–399.

Pillar, H. R., Heimbach, P., Johnson, H. L., & Marshall, D. P. (2016). Dynamical attribution of recent variability in Atlantic Overturning. *Journal of Climate*, *29*(9), 3339–3352. https://doi.org/10.1175/JCLI-D-15-0727.1

Riser, S. C., Freeland, H. J., Roemmich, D., Wijffels, S., Troisi, A., Belbéoch, M., et al. (2016). Fifteen years of ocean observations with the global Argo array. *Nature Climate Change*, *6*(2), 145–153. https://doi.org/10.1038/nclimate2872

Ritz, S. P., Stocker, T. F., Grimalt, J. O., Menviel, L., & Timmermann, A. (2013). Estimated strength of the Atlantic overturning circulation during the last deglaciation. *Nature Geoscience*, *6*(3), 208–212. https://doi.org/10.1038/ngeo1723

Roberts, C. D., & Palmer, M. D. (2012). Detectability of changes to the Atlantic meridional overturning circulation in the Hadley Centre Climate Models. *Climate Dynamics*, *39*(9), 2533–2546. https://doi.org/10.1007/s00382-012-1306-3

Schauer, U., & Beszczynska-Möller, A. (2009). Problems with estimation and interpretation of oceanic heat transport—Conceptual remarks for the case of Fram Strait in the Arctic Ocean. *Ocean Science*, *5*(4), 487–494. https://doi.org/10.5194/os-5-487-2009

Smith, T., & Heimbach, P. (2019). Atmospheric origins of variability in the South Atlantic meridional overturning circulation. *Journal of Climate*, *32*(5), 1483–1500. https://doi.org/10.1175/JCLI-D-18-0311.1

Tarantola, A. (2005). *Inverse problem theory and methods for model parameter estimation*. Philadelphia: Society for Industrial and Applied Mathematics.

Thornalley, D. J. R., Oppo, D. W., Ortega, P., Robson, J. I., Brierley, C. M., Davis, R., et al. (2018). Anomalously weak Labrador Sea convection and Atlantic overturning during the past 150 years. *Nature*, *556*(7700), 227–230. https://doi.org/10.1038/s41586-018-0007-4

Vellinga, M., & Wood, R. A. (2004). Timely detection of anthropogenic change in the Atlantic meridional overturning circulation. *Geophysical Research Letters*, *31*, L14203. https://doi.org/10.1029/2004GL020306

Verdy, A., Mazloff, M. R., Cornuelle, B. D., & Kim, S. Y. (2013). Wind-driven sea level variability on the California Coast: An adjoint sensitivity analysis. *Journal of Physical Oceanography*, *44*(1), 297–318. https://doi.org/10.1175/JPO-D-13-018.1

von Storch, H., & Zwiers, F. W. (1999). *Statistical analysis in Climate Research*. Cambridge: Cambridge University Press. https://doi.org/10.1017/CBO9780511612336

Weller, R. A., Baker, D. J., Glackin, M. M., Roberts, S. J., Schmitt, R. W., Twigg, E. S., & Vimont, D. J. (2019). The challenge of sustaining ocean observations. *Frontiers in Marine Science*, *6*, 105. https://doi.org/10.3389/fmars.2019.00105

Wunsch, C. (1996). *The ocean circulation inverse problem*. Cambridge: Cambridge University Press.

Zhang, R. (2007). Anticorrelated multidecadal variations between surface and subsurface tropical North Atlantic. *Geophysical Research Letters*, *34*, elocatorL12713. https://doi.org/10.1029/2007GL030225

Zhang, R. (2008). Coherent surface-subsurface fingerprint of the Atlantic meridional overturning circulation. *Geophysical Research Letters*, *35*, L20705. https://doi.org/10.1029/2008GL035463

Zhang, X., Prange, M., Merkel, U., & Schulz, M. (2015). Spatial fingerprint and magnitude of changes in the Atlantic meridional overturning circulation during marine isotope stage 3. *Geophysical Research Letters*, *42*, 1903–1911. https://doi.org/10.1002/2014GL063003

Zhang, W. G., Wilkin, J. L., & Levin, J. C. (2010). Towards an integrated observation and modeling system in the New York Bight using variational methods. Part II: Representer-based observing strategy evaluation. *Ocean Modelling*, *35*(3), 134–145. https://doi.org/10.1016/j.ocemod.2010.06.006